

# Unsteady aerodynamic loads on pitching aerofoils represented by Gaussian body force distributions

Emanuel Taschner<sup>1</sup> , Georgios Deskos<sup>2</sup> , Michael B. Kuhn<sup>2</sup> ,  
Jan-Willem van Wingerden<sup>1</sup> and Luis A. Martínez-Tossas<sup>2</sup>

<sup>1</sup>Delft Center for Systems and Control, Delft University of Technology, Delft, South Holland,  
The Netherlands

<sup>2</sup>National Renewable Energy Laboratory, Golden, CO, USA

**Corresponding author:** Emanuel Taschner, [e.taschner@tudelft.nl](mailto:e.taschner@tudelft.nl)

(Received 30 October 2024; revised 7 August 2025; accepted 14 October 2025)

The actuator line model (ALM) is an approach commonly used to represent lifting and dragging devices like wings and blades in large-eddy simulations (LES). The crux of the ALM is the projection of the actuator point forces onto the LES grid by means of a Gaussian regularisation kernel. The minimum width of the kernel is constrained by the grid size; however, for most practical applications like LES of wind turbines, this value is an order of magnitude larger than the optimal value that maximises accuracy. This discrepancy motivated the development of corrections for the actuator line, which, however, neglect the effect of unsteady spanwise shed vorticity. In this work we develop a model for the impact of spanwise shed vorticity on the unsteady loading of an aerofoil modelled as a Gaussian body force distribution, where the model is applicable within the regime of unsteady attached flow. The model solution is derived both in the time and frequency domain and features an explicit dependence on the Gaussian kernel width. We verify the model with ALM-LES for both pitch steps and periodic pitching. The model solution is compared with Theodorsen theory and validated with both computational fluid dynamics using body fitted grids and experiment. It is concluded that the optimal kernel width for unsteady aerodynamics is approximately 40 % of the chord. The ALM is able to predict the magnitude of the unsteady loading up to a reduced frequency of  $k \approx 0.2$ .

**Key words:** aerodynamics, general fluid mechanics

## 1. Introduction

Today's wind energy generation relies on large-scale wind farms operating optimally in the lower (surface) part of the atmospheric boundary layer (ABL) (Veers *et al.* 2019; Porté-Agel *et al.* 2020). Optimal performance of wind farms requires accurate prediction of the aerodynamic characteristics of the individual turbines and their interaction with wakes and the ambient atmospheric flow. The unsteady ABL flow is commonly computed using large-eddy simulation (LES), where wind turbines are parameterised with actuator models like actuator disks or actuator lines (Breton *et al.* 2017).

The actuator line model (ALM), initially developed by Sørensen & Shen (2002), represents lifting and dragging devices, such as blades and wings, as discrete lines. It allows for the distribution of body forces along these lines, effectively simulating the influence of solid bodies on the flow. As such, when the ALM is utilised to model a wind turbine rotor, it is capable of capturing the footprint of the individual blades and the associated vortex system composed of the bound, tip and root vortices (Troldborg 2009; Ivanell *et al.* 2010; Troldborg, Sorensen & Mikkelsen 2010; Martínez-Tossas *et al.* 2015). Nevertheless, the ALM is still relatively simple to implement thanks to its suitability with Cartesian grids. This balance between simplicity, physical accuracy and computational cost has contributed to the ALM's ongoing popularity more than twenty years after its inception (Sanderse, Pijl & Koren 2011; Breton *et al.* 2017). During these years, the ALM has enabled many advancements in wind energy and beyond, for example, the study of ABL-turbine interaction (Troldborg *et al.* 2011; Churchfield *et al.* 2012), the analysis of near-wake vortex dynamics like the tip vortex instability (Sarmast *et al.* 2014; Sørensen *et al.* 2015; Kleusberg, Benard & Henningson 2019; Hodgkin, Laizet & Deskos 2022), the study of novel wake control strategies (Yilmaz & Meyers 2018; Frederik *et al.* 2020) or the simulation of vertical axis wind turbines (Mendoza *et al.* 2019) and complex wing configurations (Kleine *et al.* 2023b).

### 1.1. Gaussian force regularisation and smearing corrections for the ALM

The accuracy of the ALM approach depends on the force projection from the discrete lines onto the LES grid using a regularisation kernel,  $\eta_\epsilon$ . In its most general form in three-dimensional space, the regularisation of a single discrete actuator point force  $f^{Act}$  across the volume  $\Omega$  takes the form

$$\mathbf{f}^{Reg} = \iiint_{\Omega} f^{Act} \eta_\epsilon \, d\mathbf{x}, \quad \mathbf{x} \in \Omega \quad \text{with } \eta_\epsilon = \frac{1}{\pi^{3/2} \epsilon^3} e^{-(|\mathbf{x}-\mathbf{x}^{Act}|)^2/\epsilon^2}, \quad (1.1)$$

where  $\epsilon$  is the Gaussian kernel width and  $\mathbf{x}^{Act}$  the actuator point location. The need for calculating a convolution of the actuator forces with a regularisation kernel was introduced in the foundational ALM work by Sørensen & Shen (2002) in order to avoid singular behaviour, which would result from direct application of the actuator point forces on the LES grid. In their work, the shape of the regularisation kernel was chosen to be an isotropic Gaussian as introduced above, where the kernel width is constant along the entire span of the blade. Motivated by the idea that the actuator forces are ultimately supposed to model the dimension and shape of the wing or blade and the associated aerofoils, a comprehensive body of literature exists aiming to improve the force regularisation accordingly (Churchfield *et al.* 2017; Martínez-Tossas *et al.* 2017; Jha & Schmitz 2018; Caprace, Chatelain & Winckelmans 2019; Schollenberger *et al.* 2020; Liu *et al.* 2022). However, independent of the employed kernel type and shape, the minimal allowable kernel width is dictated by the grid size,  $\Delta x$ , employed in LES, and arguments of a

minimum allowable ratio,  $\epsilon/\Delta x$ , have been made in order to avoid numerical oscillations and obtain convergence. Its proposed value ranges from  $\epsilon/\Delta x = 2$  (Troldborg *et al.* 2010) to  $\epsilon/\Delta x \geq 4$  (Shives & Crawford 2013) and  $\epsilon/\Delta x \geq 5$  (Martínez-Tossas *et al.* 2015).

The resulting kernel widths from grid size considerations are often an order of magnitude larger than the optimal kernel width. Martínez-Tossas *et al.* (2017) found the optimal kernel width by maximising the agreement between the two-dimensional flow solution around an aerofoil with chord,  $c$ , modelled as a Gaussian body force akin to the ALM, and the corresponding potential flow solution. They concluded that the optimal kernel width is of the order of  $\epsilon_{Opt}/c = \mathcal{O}(10^{-1})$ , which is in agreement with the earlier proposed range of  $\epsilon_{Opt}/c \in [1/8, 1/4]$  (Shives & Crawford 2013). Martínez-Tossas *et al.* (2017) further noted that the optimal kernel width is not a function of the angle of attack and that the dependence on the type of lifting surface (e.g. aerofoil camber and thickness) is weak. For the context of this work, it is also important to note that the conclusions of Martínez-Tossas *et al.* (2017) regarding the optimal kernel width were drawn considering steady-state conditions.

In practice, the existing discrepancy between the conditions for the optimal and numerically allowable kernel width is the reason why the standard ALM, when employed on coarse LES grids, fails to accurately reproduce the loading in the proximity of the wing and blade tips. One of the earliest proposals to address this issue was made by Shen, Sørensen & Mikkelsen (2005) who introduced a tip loss correction for the ALM similar to the corrections employed for blade element momentum theory. Progress has been made on this issue by Dağ & Sørensen (2020) (originally Dağ 2017), who observed that the bound vortex created by the ALM is also of Gaussian shape and, thus, similar to the shape of a Lamb–Oseen vortex. This observation was shown to be a mathematical consequence of the Gaussian force regularisation by Forsythe *et al.* (2015) for the bound vortex and by Martínez-Tossas & Meneveau (2019) for the vorticity shed by an actuator line.

These insights enable the correction of ALM results based on the mismatch between the induced velocities along the actuator line as they result from shed Lamb–Oseen vortices, with the kernel width dictated by numerical considerations and from a reference considered optimal (Martínez-Tossas & Meneveau 2019; Meyer Forsting, Pirrung & Ramos-García 2019a; Dağ & Sørensen 2020; Kleine *et al.* 2023a). These corrections – also often labelled as smearing corrections – were applied to wind turbine rotors, for example, by Meyer Forsting *et al.* (2019b), Stanly *et al.* (2022) and Taschner *et al.* (2024). Meyer Forsting *et al.* (2019a) and Kleine *et al.* (2023a) also tested their corrections for unsteady operating conditions, namely the NREL 5 MW turbine subject to a step in blade pitch or operating in sheared inflow. In these conditions, spanwise vorticity would also be shed in response to the varying strength of the bound vortex. The effect of this additional unsteady vorticity component is not captured by the previously mentioned corrections, which also neglect the influence of drag. Kleine *et al.* (2023a) pointed out in their work that a better understanding of drag and unsteady effects and their relation to the error caused by Gaussian regularisation with large kernel widths could help to further decrease associated errors. The impact of drag was already studied in the work of Caprace, Winckelmans & Chatelain (2020), who developed an immersed lifting and dragging line method, which captures streamwise/spanwise and normal/spanwise shed vorticity for lift and drag forcing, respectively.

### 1.2. Unsteady aerodynamics in the context of the ALM

The previous outline shows that progress has been made on developing the ALM, and theoretical insights lead to corrections for practically employed kernel widths.

These developments mostly focused on steady and quasi-steady conditions. The operating conditions of a wind turbine are, however, subject to various periodic and aperiodic sources of unsteadiness like shear, veer and high-frequency turbulence fluctuations in the atmospheric inflow; body motion due to flexible structures; tower shadow effects; and interaction of the blades with wakes generated by upstream turbines (Leishman 2002a). There also exists a variety of wind farm control strategies to mitigate wake effects on downstream turbines. These wake control strategies utilise the turbine's yaw, rotational and pitch degrees of freedom, often introducing additional sources of unsteadiness (Meyers *et al.* 2022).

The body force approach of the ALM is at the core of its simplicity, and therefore, it may not resolve phenomena associated with boundary-layer dynamics, e.g. flow separation/reattachment, laminar–turbulent transition and dynamic stall effects. Their effect on the unsteady lift and drag can only be included by means of additional models, e.g. the dynamic stall model from Leishman & Beddoes (1989). However, even for flow scenarios corresponding to unsteady attached flow, the question remains of how Gaussian force regularisation with suboptimal large kernel widths may impact the unsteady loading. When using suboptimal large kernel widths the vorticity shed in response to the wake suffers from an excess of smearing, similar to the steady case, affecting its feedback to the angle of attack (induction) and, thus, the loading on the blades. The role of shed unsteady spanwise vorticity has so far been neglected from previous ALM corrections (Martínez-Tossas & Meneveau 2019; Meyer Forsting *et al.* 2019a; Dağ & Sørensen 2020; Kleine *et al.* 2023a), and therefore, it is the focus of this study.

We begin by tackling the unsteady two-dimensional incompressible, inviscid flow over a Gaussian body force, similar to the successive theoretical advancements of the ALM in steady conditions (Martínez-Tossas *et al.* 2017). This approach links the unsteady two-dimensional ALM (or actuator point rather than actuator line) to the wealth of foundational work on the unsteady incompressible, inviscid thin-aerofoil problem (von Kármán & Sears 1938; Bisplinghoff, Ashley & Halfman 1996; Leishman 2002b). Unsteady inviscid solutions can be traced back to the pioneering work of Prandtl (1924). They noted that unsteady aerofoil loading implies the shedding of circulation into the wake and suggested a first-order solution to the problem of a flapping aerofoil. Birnbaum (1924) solved this problem by utilising a series approximation and quantified the degree of unsteadiness with the so-called reduced frequency,  $k$ , a non-dimensional number given by the ratio of the time scales of the unsteady phenomena and the time needed by the flow to travel across the aerofoil's semi-chord length. Since a number of solutions have been derived to address the unsteady thin-aerofoil problem, it is helpful to categorise them based on two criteria (Leishman 2002b): firstly, whether the solution is derived in the time or frequency domain, and secondly, whether the source of unsteadiness is the inflow (e.g. sinusoidal gusts of the normal velocity) or the aerofoil motion, e.g. translatory oscillation (heave) and/or rotational oscillation (pitching). Wagner (1925) and Küssner (1936) derived time domain solutions for the cases of unsteady body motion and unsteady inflow, respectively. Corresponding frequency domain solutions were derived by Theodorsen (1935) for the case of aerofoil motion and by Sears (1941) for gusts.

In either case, the lift can be split into three contributions: (i) quasi-steady, (ii) apparent-mass and (iii) wake-induced (von Kármán & Sears 1938; Sears 1941). The computation of contribution (iii) is based on the transfer functions  $C(k)$  and  $S(k)$  for Theodorsen's and Sears's solutions, respectively. These transfer functions incorporate the frequency-dependent phase and magnitude modulation of the unsteady lift caused by the shed vorticity in the wake. In principle, the ALM inherently captures the wake-induced

unsteady loading since it is modelled by the LES. However, this also raises the following three fundamental questions.

- (i) Does the optimal kernel width determined for steady-state conditions still apply to the unsteady case?
- (ii) How does the error in the unsteady loading depend on  $\epsilon_*$  and  $k$  when employing suboptimal large kernel widths?
- (iii) Beyond which reduced frequencies does the ALM fail to accurately model unsteady aerodynamics even when employing the optimal kernel width and considering attached flow conditions below stall?

### 1.3. Objective

The present work tackles these questions for the case of unsteady attached flow over a pitching aerofoil modelled as a two-dimensional Gaussian body force, i.e. the unsteady two-dimensional ALM. The detailed contributions are as follows.

- (i) The development of a first-order model capable of reproducing two-dimensional unsteady ALM results without relying on the use of LES. The model is formulated in the time and frequency domain, akin to the aerodynamic models of Wagner (1925) and Theodorsen (1935), but stems from a formulation of the governing equations that is consistent with the ALM.
- (ii) The establishment of a range for the optimal Gaussian kernel width for the ALM in the case of unsteady aerodynamics by comparing the model with inviscid computational fluid dynamics (CFD) using body fitted grids and Theodorsen theory.
- (iii) The identification of a threshold reduced frequency beyond which the ALM fails to accurately capture the unsteady aerofoil loading even when employing the optimal kernel width for unsteady conditions from (ii). This identification is based on numerical and experimental validation data and a detailed comparison with Theodorsen theory.

The remainder of the paper is organised as follows. We start by formulating the unsteady two-dimensional problem and derive its general solution in terms of vorticity in § 2. In § 3 we then utilise the derived unsteady vorticity solution to obtain the corresponding induced velocity solution at the aerofoil location by means of the Biot–Savart law. Section 4 builds upon the induced velocity solutions to obtain a model for the unsteady aerofoil loading both in the time and frequency domain, where the latter is compared in detail to Theodorsen theory. We verify the model predictions for the aerofoil’s unsteady loading by comparing them to ALM-LES in § 5 and discuss the impact of neglecting nonlinear contributions for the model derivation in § 6. In § 7 the model is validated with numerical and experimental benchmarks to establish the range of the optimal kernel width for unsteady aerodynamics and identify the limits of the ALM’s applicability. We conclude with § 8, where the findings are summarised and an outlook of future work is provided.

## 2. Flow over an unsteady two-dimensional Gaussian body force

We start by deriving the general solution for the unsteady vorticity field that forms around an aerofoil represented by a two-dimensional Gaussian body force. For the derivations, we assume incompressible flow in the infinite-Reynolds-number limit. Following the work of Martínez-Tossas *et al.* (2017), but retaining the time-derivative term, our starting point is the two-dimensional unsteady Euler equation in non-dimensional form. We use

the free-stream velocity,  $U_\infty$ , the fluid density,  $\rho$ , and the aerofoil's chord length,  $c$ , as the characteristic velocity, density and length scales, respectively, and define the dimensionless time and space coordinates  $t_* = tU_\infty/c$ ,  $x_* = x/c$ ,  $y_* = y/c$ ,  $\epsilon_* = \epsilon/c$ , velocities  $u_* = u/U_\infty$ ,  $v_* = v/U_\infty$ , pressure  $p_* = p/(\rho U_\infty^2)$  and vorticity  $\omega_* = \omega c/U_\infty$  to obtain

$$\frac{\partial \mathbf{u}_*}{\partial t_*} + \mathbf{u}_* \cdot \nabla_* \mathbf{u}_* = -\nabla_* p_* - \frac{C_x \mathbf{i} + C_y \mathbf{j}}{2\pi\epsilon_*^2} e^{-(x_*^2+y_*^2)/\epsilon_*^2}, \quad (2.1)$$

where  $\mathbf{u}_* = (u_*, v_*)^\top$  is the velocity vector and  $\mathbf{i}$  and  $\mathbf{j}$  represent the streamwise and normal unit vectors. Here, the non-dimensional streamwise forcing,  $C_x$ , and normal forcing,  $C_y$ , model the impact of the aerofoil on the flow akin to the ALM. The force coefficients are functions of the time-dependent angle of attack  $\alpha(t_*)$  and are regularised with a Gaussian kernel of width,  $\epsilon_*$ , centred at the actuator point located at  $\mathbf{x}_*^{Act} = (x_*^{Act}, y_*^{Act})^\top = (0, 0)^\top$ . By taking the curl of (2.1), the pressure term can be eliminated, and we obtain a transport equation for the vorticity,

$$\frac{\partial \omega_*}{\partial t_*} + \mathbf{u}_* \cdot \nabla_* \omega_* = \frac{-y_* C_x + x_* C_y}{\pi \epsilon_*^4} e^{-(x_*^2+y_*^2)/\epsilon_*^2}. \quad (2.2)$$

Equation (2.2) may further be simplified by considering a linear perturbation analysis around  $\omega_* = 0$ , and thus,  $C_x = C_y = 0$  such that  $\mathbf{u}_* = \mathbf{i} + \mathbf{u}_*^p$ ,  $\omega_* = \omega_*^p$ ,  $C_x = C_x^p$ ,  $C_y = C_y^p$  and  $\mathbf{u}_* \cdot \nabla_* \omega_* \approx \partial \omega_*^p / \partial x_*$ . After these approximations, (2.2) becomes

$$\frac{\partial \omega_*^p}{\partial t_*} + \frac{\partial \omega_*^p}{\partial x_*} = \frac{-y_* C_x^p + x_* C_y^p}{\pi \epsilon_*^4} e^{-(x_*^2+y_*^2)/\epsilon_*^2}. \quad (2.3)$$

For the remainder of this paper, the superscripts  $p$  are omitted for all variables and it is understood that they refer to their respective perturbation values. It should be noted that the linearisation point of  $\omega_* = 0$  implicitly assumes an infinitesimally thin non-cambered drag-free aerofoil at zero mean angle of attack such that the wake of the aerofoil lies on the  $x$  axis at  $y_* = 0$  parallel to the free-stream velocity  $U_\infty$ . Thus, applying the derived solutions to aerofoils with a non-zero base loading, camber or thickness is an approximation since the influence of mean-flow deflection on the vorticity transport is neglected. The first effect will be observed when compared with the nonlinear LES reference in § 5, whereas the latter two aspects are inherently not captured by the ALM and, thus, also not present in the nonlinear LES results. More advanced second-order approaches would be needed to take those effects into account, as for the example in the Sears problem (Goldstein & Atassi 1976; Atassi 1984). The impact of the simplifying assumptions made here to arrive at the linearised vorticity transport (2.3) is discussed in § 6. It should be noted that the assumptions made are shared with the theory of Theodorsen (1935) (see, e.g. Limacher 2025). In particular, the modelling approach taken here is valid as long as the considered flow conditions correspond to unsteady attached flow across the aerofoil.

Using the streamwise and normal perturbation velocities, one can define the flow angle at the actuator point  $\phi = \arctan(v_*/(1+u_*))$ . The flow angle is related to the angle of attack via the pitch angle  $\beta$  as  $\alpha = \phi + \beta$ , where we consider in this work the unsteady forcing to stem from a time-dependent pitch angle,  $\beta(t_*)$ . It should be stressed that the angle of attack not only depends on the pitch angle, but also via the flow angle/the perturbation velocities on the unsteady vorticity field  $\omega_*(x_*, y_*, t_*)$ , i.e. the solution of (2.3). Hence, the unsteady forcing term on the right-hand side of (2.3) is not known *a priori*. It instead follows from solving the underlying feedback problem between the unsteady loading and the unsteady shed vorticity in the aerofoil wake, which can be

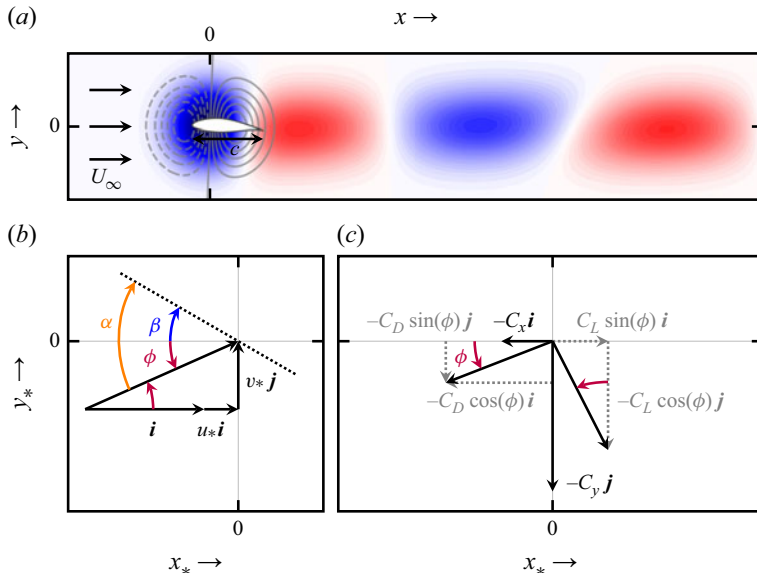


Figure 1. (a) The problem set-up with the pitching aerofoil (chord  $c$ ) represented by a two-dimensional Gaussian body force in a free stream flow of speed  $U_\infty$ . The resulting unsteady vorticity source term (right-hand side of the vorticity transport equation (2.3)) is illustrated by the grey dashed/solid (negative/positive vorticity source term) contour lines. The small tilt angle of the contour is caused by the source term contribution of the streamwise forcing  $C_x$ . The blue/red (negative/positive vorticity) contours illustrate the resulting bound vortex and shed vorticity. Note that the vorticity source term and the vorticity are time dependent, and thus, their signs and magnitudes at a given spatial location can change. (b) Definition of the angle of attack,  $\alpha$ , pitch angle,  $\beta$ , flow angle,  $\phi$  and the velocity vector at the actuator point,  $(x_*^{\text{Act}}, y_*^{\text{Act}})^\top = (0, 0)^\top$ . (c) Definition of the streamwise  $C_x$  and normal  $C_y$  force coefficients and their relation to the lift  $C_L$  and drag  $C_D$  coefficients. Note that all force coefficients are expressed as force acting from the body on the fluid. Furthermore, the magnitude of the drag force is exaggerated to aid the visual presentation of the projection.

formulated in terms of the flow angle as we show in § 4. The flow angle furthermore allows us to determine the streamwise and normal force coefficients from the aerofoil-specific tabulated lift  $C_L$  and drag  $C_D$  coefficients according to the projections

$$\begin{aligned} C_x &= -C_L \sin(\phi) + C_D \cos(\phi), \\ C_y &= C_L \cos(\phi) + C_D \sin(\phi). \end{aligned} \quad (2.4)$$

While the force coefficient time histories are determined by a look-up operation from a static aerofoil-specific table using the instantaneous angle of attack, the unsteadiness enters the problem via the aforementioned feedback problem, whose solution determines the angle of attack time history. This is consistent with the approach taken in Theodorsen theory, where the unsteady circulatory lift follows from the quasi-steady one via a modified angle of attack due to the unsteady shed vorticity (Theodorsen 1935). For Theodorsen theory, the underlying employed static lift coefficient taken as input is that of the flat plate aerofoil,  $C_L = 2\pi\alpha$ , which follows from thin-aerofoil theory and, in particular, the use of the Kutta condition and the Kutta–Joukowski theorem (Batchelor 1967; Milne-Thomson 1973). The problem set-up together with the definitions of the coordinate system, the velocity vector, the angles and the force projection are visualised in figure 1.

Equation (2.3) is a linear non-homogeneous partial differential equation and can be solved using the method of characteristics (see Appendix A). The solution for  $t_* \geq 0$  is given by

$$\begin{aligned} \omega_*(x_*, y_*, t_*) &= \omega_*^{IC}(x_* - t_*, y_*) \\ &+ \underbrace{\int_0^{t_*} \frac{-y_* C_x(s) + (x_* + s - t_*) C_y(s)}{\pi \epsilon_*^4} e^{-((x_* + s - t_*)^2 + y_*^2)/\epsilon_*^2} ds}_{\omega_*^{us}(x_*, y_*, t_*)}. \end{aligned} \quad (2.5)$$

The solution comprises two terms. The first term,  $\omega_*^{IC}$ , is the initial condition representing a spatio-temporal shift,  $x_* - t_* = (x - U_\infty t)/c$ , due to vorticity being advected by the free-stream velocity,  $U_\infty$ , and the second term,  $\omega_*^{us}$ , captures the generation of shed vorticity due to the fluctuations of the unsteady forcing term (unsteady streamwise and normal Gaussian body forces). Equation (2.5) allows us to solve for the two-dimensional time-dependent vorticity field. However, if one is interested in a solution not expressed in terms of a time integral, the forcing needs to be expressed in terms of a given set of basis functions. In Appendix B we derive such a solution by expressing the forcing in terms of a Fourier series. However, here we turn our attention towards deriving solutions for the induced velocity along the wake centreline  $(x_*, y_* = 0)^\top$  since the knowledge of the induced velocity at the actuator point  $(x_*^{Act}, y_*^{Act})^\top = (0, 0)^\top$  is sufficient to compute the unsteady loading on the aerofoil.

### 3. The induced velocity due to unsteady forcing

The solution for the induced velocity at location  $\mathbf{x} = (x_*, y_*)^\top$  due to vorticity residing at  $\mathbf{x}' = (x'_*, y'_*)^\top$  can be derived by applying the Biot–Savart law (Saffman 1992) to the general unsteady vorticity solution (2.5), which for the given two-dimensional flow, reads as

$$(u_*, v_*)^\top = \frac{1}{2\pi} \int_{-\infty}^{+\infty} \int_{-\infty}^{+\infty} \omega_*(x'_*, y'_*, t_*) \frac{-(y_* - y'_*)\mathbf{i} + (x_* - x'_*)\mathbf{j}}{(x_* - x'_*)^2 + (y_* - y'_*)^2} dx'_* dy'_*. \quad (3.1)$$

We note that when seeking a solution restricted to the wake centreline for the linearised equations, the streamwise forcing only induces streamwise velocity perturbations and the normal forcing only induces normal velocity perturbations. Hence, only one velocity component of the Biot–Savart integral needs to be evaluated for each forcing direction.

#### 3.1. Induced velocity due to normal forcing

The normal induced velocity along the wake centreline  $(x_*, y_* = 0)^\top$  is obtained by solving the normal component of the Biot–Savart integral given in (3.1) for a generic normal forcing  $C_y(t_*)$ . First, we focus here on the contribution from the second term of the unsteady vorticity solution  $\omega_*^{us}$  (the time integral in (2.5)). By switching the order of temporal and spatial integration, we may obtain

$$v_*^{us}(x_*, 0, t_*) = \int_0^{t_*} \frac{1}{2\pi} \int_{-\infty}^{+\infty} \int_{-\infty}^{+\infty} \frac{(x_* - x'_*)(x'_* + s - t_*)}{(x_* - x'_*)^2 + (-y'_*)^2} \frac{C_y(s)}{\pi \epsilon_*^4} e^{-((x'_* + s - t_*)^2 + y'^2)/\epsilon_*^2} dx'_* dy'_* ds, \quad (3.2)$$

which is the normal perturbation velocity induced by the vorticity shed as a result of the unsteady forcing in the time interval  $t_* \in [0, t_*]$ . Integration in the two spatial directions leads to

$$v_*^{us}(x_*, 0, t_*) = \int_0^{t_*} \frac{-C_y(s)}{2\pi} \left[ \frac{e^{-(x_* + s - t_*)^2/\epsilon_*^2}}{\epsilon^2} + \frac{e^{-(x_* + s - t_*)^2/\epsilon_*^2} - 1}{2(x_* + s - t_*)^2} \right] ds. \quad (3.3)$$

We note that the integrand in the limit  $(x_* + s - t_*) \rightarrow 0$  tends to  $-C_y(s)/(4\pi\epsilon_*^2)$ , i.e. it is not singular. The derived solution shows the identical structure as the formula obtained by Martínez-Tossas *et al.* (2024) for their generalised steady three-dimensional filtered lifting line theory. This equivalence stems from the fact that the two problems are similar upon applying a rotation of 90° to their coordinate system and replacing the spatial convolution integral in their solution with a spatio-temporal convolution as in (3.3). So far, only the contribution from the second term of the vorticity solution  $\omega_*^{us}$  has been considered. Thus, the induced velocity solution in (3.3) has to be complemented with a term  $v_*^{IC}(x_*, 0, t_*)$ , accounting for the velocity induced by the initial vorticity field in case  $\omega_*^{IC} \neq 0$  in (2.5). If we assume that the initial condition is given by the steady-state solution of the flow over a Gaussian body force, one can take the initial condition derived by Martínez-Tossas *et al.* (2017), i.e. the velocity field induced by a Lamb–Oseen vortex with core size  $\epsilon_*$  advected downstream by the background flow:

$$v_*^{IC}(x_* - t_*, 0) = \frac{-C_y(t_* = 0)}{4\pi} \frac{1 - e^{-((x_* - t_*)/\epsilon_*)^2}}{x_* - t_*}. \quad (3.4)$$

The complete solution for the normal induced velocity along the wake centreline follows by combining (3.3) and (3.4) as

$$v_*(x_*, 0, t_*) = v_*^{IC}(x_* - t_*, 0) + v_*^{us}(x_*, 0, t_*). \quad (3.5)$$

While for numerical implementation purposes the structure of the solution in (3.3) is beneficial since it does not require the calculation of the temporal gradient of  $C_y(t_*)$ , it is insightful to rewrite the time integral using integration by parts, i.e.

$$\begin{aligned} v_*^{us}(x_*, 0, t_*) &= - \left[ \frac{C_y(s)}{4\pi} \frac{1 - e^{-((x_* + s - t_*)/\epsilon_*)^2}}{x_* + s - t_*} \right]_{s=0}^{s=t_*} \\ &\quad + \int_0^{t_*} \frac{1}{4\pi} \frac{dC_y(s)}{ds} \frac{1 - e^{-((x_* + s - t_*)/\epsilon_*)^2}}{x_* + s - t_*} ds, \end{aligned} \quad (3.6)$$

where we define the indicial response function as

$$\varphi(x_* + s - t_*) = \frac{1 - e^{-((x_* + s - t_*)/\epsilon_*)^2}}{x_* + s - t_*}. \quad (3.7)$$

In the steady case ( $dC_y/ds = 0$ ), the time integral vanishes, and the term in the first brackets evaluated for the lower bound  $s = 0$  cancels the initial condition in (3.4). Thus, the only remaining term is the first term evaluated at the upper integration bound, which represents the induced velocity of the bound vortex, e.g. one recovers the solution of the steady problem.

When combining the contributions of the vorticity initial condition (3.4) and the vorticity due to unsteady forcing (3.6) to the normal induced velocity at the actuator point as  $v_*(0, 0, t_*) = v_*^{IC}(0 - t_*, 0) + v_*^{us}(0, 0, t_*)$ , we obtain the solution

$$v_*(0, 0, t_*) = - \int_0^{t_*} \frac{1}{4\pi} \frac{dC_y(s)}{ds} \varphi(t_* - s) ds, \quad (3.8)$$

where we exploit the fact that  $\varphi(x_* + s - t_*)$  for  $x_* = 0$  is an anti-symmetric function and  $\varphi(0) = 0$ . This solution is a Duhamel's integral with the indicial response function  $\varphi$  (Leishman 2002b). The induced velocity at the actuator point at time  $t_*$  due to the unsteady Gaussian forcing is then obtained as the superposition of all indicial responses to the forcing in the time interval  $s \in [0, t_*]$ . Wagner (1925) derived an indicial response function for the response of a thin aerofoil to a step change of the angle of attack, which has been shown by Garrick (1938) to be directly related to Theodorsen's function  $C(k)$  in the frequency domain (Theodorsen 1935). In our case, the indicial response function for an unsteady Gaussian forcing is parameterised with the Gaussian kernel width  $\epsilon_*$ , and from (3.7) it can be seen that the indicial response function is given by the shape representative for the induced velocity of a Lamb–Oseen vortex with core size  $\epsilon_*$  located at the streamwise location  $x_* = t_* - s$ .

### 3.2. Induced velocity due to streamwise forcing

The streamwise induced velocity along the wake centreline  $(x_*, y_* = 0)^\top$  is obtained by solving the streamwise component of the Biot–Savart integral given in (3.1) for a generic streamwise forcing  $C_x(t)$ . We first focus again on the contribution from the second term of the unsteady vorticity solution  $\omega_*^{us}$  (the time integral in (2.5)). By switching the order of temporal and spatial integration, it follows that

$$u_*^{us}(x_*, 0, t_*) = - \int_0^{t_*} \frac{1}{2\pi} \int_{-\infty}^{+\infty} \int_{-\infty}^{+\infty} \frac{(-y'_*)}{(x_* - x'_*)^2 + (-y'_*)^2} \frac{-y'_* C_x(s)}{\pi \epsilon_*^4} e^{-((x'_* + s - t_*)^2 + y'^2_*)/\epsilon_*^2} dx'_* dy'_* ds \quad (3.9)$$

and the two integrals in  $x'_*$  and  $y'_*$  can be solved analytically to obtain

$$u_*^{us}(x_*, 0, t_*) = \int_0^{t_*} \frac{C_x(s)}{4\pi} \left[ \frac{e^{-(x_* + s - t_*)^2/\epsilon_*^2} - 1}{(x_* + s - t_*)^2} \right] ds. \quad (3.10)$$

It should be noted that in the limit case of a vanishing spatio-temporal shift  $x_* + s - t_* \rightarrow 0$ , the integrand tends to  $-C_x(s)/(4\pi \epsilon_*^2)$ .

Furthermore, given the assumption of constant streamwise forcing  $C_x \neq C_x(t_*)$ , one can recover the induced velocity solution of the steady two-dimensional problem derived by Martínez-Tossas *et al.* (2017). We derive here the solution valid for any  $x_*$ , but restricted to  $y_* = 0$ . To this end, (3.10) is integrated for general  $t_*$  but constant  $C_x$ , which yields

$$u_*^{us}(x_*, 0, t_*) = \frac{C_x}{4\pi} \left[ \frac{1 - e^{-(x_* + s - t_*)^2/\epsilon_*^2}}{(x_* + s - t_*)} - \frac{\sqrt{\pi}}{\epsilon_*} \operatorname{erf}\left(\frac{(x_* + s - t_*)}{\epsilon_*}\right) \right]_{s=0}^{s=t_*}. \quad (3.11)$$

The steady-state solution along the curve  $(x_*, y_* = 0)^\top$  is obtained in the limit  $t_* \rightarrow \infty$  using the rule of l'Hôpital:

$$u_*^{st}(x_*, 0) = \frac{C_x}{4\pi} \left[ \frac{1 - e^{-x_*^2/\epsilon_*^2}}{x_*} - \frac{\sqrt{\pi}}{\epsilon_*} \operatorname{erf}\left(\frac{x_*}{\epsilon_*}\right) - \frac{\sqrt{\pi}}{\epsilon_*} \right]. \quad (3.12)$$

In the case of  $x_* \rightarrow \infty$ , the first term vanishes and the error function tends to one that leads to a limit value of  $u_*^{st}(y_* = 0) = -C_x/(2\sqrt{\pi} \epsilon_*)$  far downstream, which is exactly the result

derived by Martínez-Tossas *et al.* (2017). Furthermore, at the actuator point the solution is exactly half of the limit value far downstream, i.e.  $u_*^{SI}(y_* = 0) = -C_x/(4\sqrt{\pi}\epsilon_*)$ . Similar to the normal forcing case, the solution in (3.12) can also be used as an initial condition in order to account for a non-zero initial vorticity field  $\omega_*^{IC}(x_* - t_*, y_*)$  due to streamwise forcing, i.e.

$$u_*^{IC}(x_* - t_*, 0) = \frac{C_x(t_* = 0)}{4\pi} \left[ \frac{1 - e^{-(x_* - t_*)^2/\epsilon_*^2}}{x_* - t_*} - \frac{\sqrt{\pi}}{\epsilon_*} \operatorname{erf}\left(\frac{x_* - t_*}{\epsilon_*}\right) - \frac{\sqrt{\pi}}{\epsilon_*} \right]. \quad (3.13)$$

The complete solution for the normal induced velocity along the wake centreline then follows by combining (3.10) and (3.13) as

$$u_*(x_*, 0, t_*) = u_*^{IC}(x_* - t_*, 0) + u_*^{us}(x_*, 0, t_*). \quad (3.14)$$

#### 4. A model for the unsteady aerofoil loading

In §§ 3.1 and 3.2 the time-dependent solutions for the normal and streamwise induced velocity due to an unsteady Gaussian body force are derived, which allow us to define the velocity sampled at the actuator point  $(x_*^{Act}, y_*^{Act})^\top = (0, 0)^\top$ . These formulas will now be used to combine the velocity solutions with the forcing time histories. The forcing time histories  $C_x(t_*)$  and  $C_y(t_*)$  are functions of the external pitch angle input and of the induced velocities since they change the flow angle and, thus, in turn, the forcing. This feedback turns the velocity solutions given by (3.5) and (3.14) into integral equations. The associated feedback problem can be formulated in terms of the flow angle, and its solution can be found in either the time (§ 4.1) or frequency (§ 4.2) domain in order to obtain a model for the unsteady loading of the aerofoil modelled as a Gaussian body force.

##### 4.1. Time domain solution: the root-finding problem

We now seek to obtain the time history of both the forcing and the velocity at the actuator point as a function of time using (3.5) and (3.14). We write the time history of the velocity at the actuator point with a single equation in terms of the flow angle, as done by Ning (2014) and Martínez-Tossas *et al.* (2024). The tangent of the flow angle at the actuator point is defined by

$$\tan(\phi(t_*)) = \frac{v_*(0, 0, t_*)}{1 + u_*(0, 0, t_*)}, \quad (4.1)$$

where  $u_*$  and  $v_*$  can both be written in terms of  $\phi$ ; thus, this is an implicit equation where the time history,  $\phi(t_*)$ , is the only unknown. Rearranging (4.1) yields

$$R(\phi) = v_*(0, 0, t_*) \cos(\phi) - (1 + u_*(0, 0, t_*)) \sin(\phi) = 0. \quad (4.2)$$

Given a guess for  $\phi(t_*)$  as input, the following algorithm provides the steps to compute (4.2).

- (i) Compute the angle of attack using the known pitch input,  $\beta(t_*)$ :

$$\alpha(t_*) = \phi(t_*) + \beta(t_*). \quad (4.3)$$

- (ii) This effective angle of attack, which incorporates the effect of the shed vorticity, allows for the evaluation of the lift,  $C_L(\alpha(t_*))$ , and drag,  $C_D(\alpha(t_*))$ , coefficients from tabulated aerofoil data, which can be subsequently converted into the corresponding streamwise and normal forcing coefficients using the projection based on the flow

angle given in (2.4):

$$C_x(t_*) = -C_L(t_*) \sin(\phi(t_*)) + C_D(t_*) \cos(\phi(t_*)), \quad (4.4)$$

$$C_y(t_*) = C_L(t_*) \cos(\phi(t_*)) + C_D(t_*) \sin(\phi(t_*)). \quad (4.5)$$

(iii) The integral equations for the induced velocities are solved via numerical integration:

$$u_*(0, 0, t_*) = u_*^{IC}(0 - t_*, 0) + \int_0^{t_*} \frac{C_x(s)}{4\pi} \left[ \frac{e^{-(s-t_*)^2/\epsilon_*^2} - 1}{(s - t_*)^2} \right] ds, \quad (4.6)$$

$$v_*(0, 0, t_*) = v_*^{IC}(0 - t_*, 0) + \int_0^{t_*} -\frac{C_y(s)}{2\pi} \left[ \frac{e^{-(s-t_*)^2/\epsilon_*^2}}{\epsilon_*^2} + \frac{e^{-(s-t_*)^2/\epsilon_*^2} - 1}{2(s - t_*)^2} \right] ds. \quad (4.7)$$

(iv) Finally, the residual is computed:

$$R(\phi) = v_*(0, 0, t_*) \cos(\phi) - (1 + u_*(0, 0, t_*)) \sin(\phi). \quad (4.8)$$

A multidimensional root-finding algorithm then iteratively evaluates steps (i)–(iv) to compute the  $\phi(t_*)$  that solves  $R(\phi(t_*)) = 0$ . The resulting  $\phi(t_*)$  is the full solution to the problem that provides the time history of forcing at the actuator point. The algorithm above is implemented based on the python `scipy.optimize.root()` function (Virtanen *et al.* 2020) using the derivative-free spectral algorithm for nonlinear equations (DF-SANE) by La Cruz *et al.* (2006).

#### 4.2. Frequency domain solution: the closed-loop transfer function

The time domain solution from § 4.1 can be compared with results from ALM-LES. However, it is insightful to also formulate the feedback problem in the frequency domain since it allows for a concise analysis of the Gaussian kernel width's influence on the phase and magnitude modulation of the unsteady loading through a closed-loop transfer function. This connection is analogous to the one that can be obtained between Theodorsen's frequency domain solution for unsteady aerofoil motion (Theodorsen 1935) and Wagner's time domain solution (Wagner 1925) as shown by Garrick (1938).

In order to derive the transfer function from the quasi-steady to the unsteady lift, we explicitly need to linearise the projection of the lift and drag coefficients onto the streamwise and normal directions (2.4), which is not necessary for the time-domain solution. When doing so, one obtains  $C_y \approx C_L + C_D\phi$ , and since  $C_D$  is at least an order of magnitude smaller than  $C_L$  in the operating regime of interest for this study, it is consistent to neglect the drag because  $C_D\phi$  is a higher-order term. The linearised lift coefficient is then described by its value at the linearisation point,  $C_L(\beta^0)$ , and the corresponding lift slope  $dC_L/d\alpha(\beta^0)$ . For a given sinusoidal pitch input signal  $\beta(t_*) = \beta^0 + \Delta\beta \sin(2kt_*)$  with amplitude  $\Delta\beta$ , the quasi-steady and unsteady lift coefficients are then, after the decay of any transient, given by

$$C_L^{qs}(t_*; k) = C_L(\beta^0) + \Delta\beta \sin(2kt_*) \left. \frac{dC_L}{d\alpha} \right|_{\beta^0}, \quad (4.9)$$

$$C_L^{us}(t_*; k) = C_L(\beta^0) + \Delta\beta |G(k)| \sin(2kt_* + \angle G(k)) \left. \frac{dC_L}{d\alpha} \right|_{\beta^0}, \quad (4.10)$$

where  $|G|$  and  $\angle G$  are the magnitude and phase of the corresponding closed-loop transfer function  $G$  mapping from the quasi-steady to the unsteady lift. This transfer function can

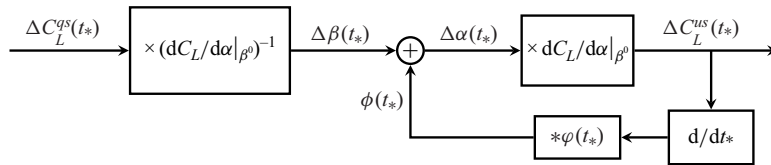


Figure 2. Schematic block diagram of the feedback problem for the unsteady lift experienced by a pitching aerofoil with  $C_D = 0$  at a linearised operating point  $\beta^0$ . The convolution operator is denoted by  $*$  and  $\varphi$  is the indicial response function for the normal induced velocity (defined in (3.7)).

be derived from the system's block diagram shown in figure 2, where we invoke the small-angle approximation for the flow angle  $\phi \approx v_*$ . Calculating the Laplace transform of the individual blocks, the transfer function follows from block diagram algebra. It should be noted that the Laplace transform has the convenient property that the convolution of two functions in the time domain reduces simply to a multiplication in the Laplace domain. Denoting the Laplace transform of the indicial response function  $\varphi$  for the normal induced velocity defined in (3.7) as  $\Phi(ik)$ , the closed-loop transfer function for the feedback problem then reads as

$$G(k) = \frac{\Delta C_L^{us}(k)}{\Delta C_L^{qs}(k)} = \frac{1}{1 - 2ki \left. \frac{dC_L}{d\alpha} \right|_{\beta^0} \Phi(ik)}, \quad (4.11)$$

with  $i$  denoting the imaginary unit (not to be confused with the streamwise unit vector  $\hat{i}$ ). The full expression for the Laplace transform of the indicial response function  $\varphi$  is given by

$$\Phi(ik) = \frac{1}{16\pi} \left[ 2\gamma - 2\pi \operatorname{erfi}(ik\epsilon_*) - 2 \log(1/\epsilon_*^2) + 4 \log(2ki) + (2\epsilon_* ki)^2 {}_2F_2((1, 1); (3/2, 2); (ik\epsilon_*)^2) \right], \quad (4.12)$$

where  $\gamma$  is Euler's constant and  ${}_pF_q(a; b; z)$  is the generalised hypergeometric function. Unsteady aerodynamics problems are commonly classified using the reduced frequency  $k = \pi f c / U_\infty$ , which is based on the semi-chord length (Leishman 2002b). Recalling that the non-dimensional variables in this work are based on the chord length and the free-stream velocity, it follows that the angular frequency is given by  $\sigma_* = 2k$ , which explains the added factor of 2 when writing the frequency in terms of the reduced frequency  $k$ .

#### 4.3. Relation between $G(k)$ and Theodorsen theory

Theodorsen (1935) derived a transfer function  $T(k)$  from quasi-steady to unsteady lift for a flat plate aerofoil modelled as a line distribution of point vortices. For an aerofoil in pure pitching motion, it consists of two non-circulatory (apparent mass)  $T_{NC}(k)$  and two circulatory  $T_C(k)$  contributions given by

$$\begin{aligned} T(k) &= \frac{\Delta C_L^{us}(k)}{\Delta C_L^{qs}(k)} = T_{NC}(k) + T_C(k) = \left[ T_{NC}^\beta(k) + T_{NC}^{\ddot{\beta}}(k) \right] + \left[ T_C^\beta(k) + T_C^{\dot{\beta}}(k) \right] \\ &= \frac{[\pi ik + \pi ak^2] + 2\pi C(k) \left[ 1 + ik(\frac{1}{2} - a) \right]}{2\pi}, \end{aligned} \quad (4.13)$$

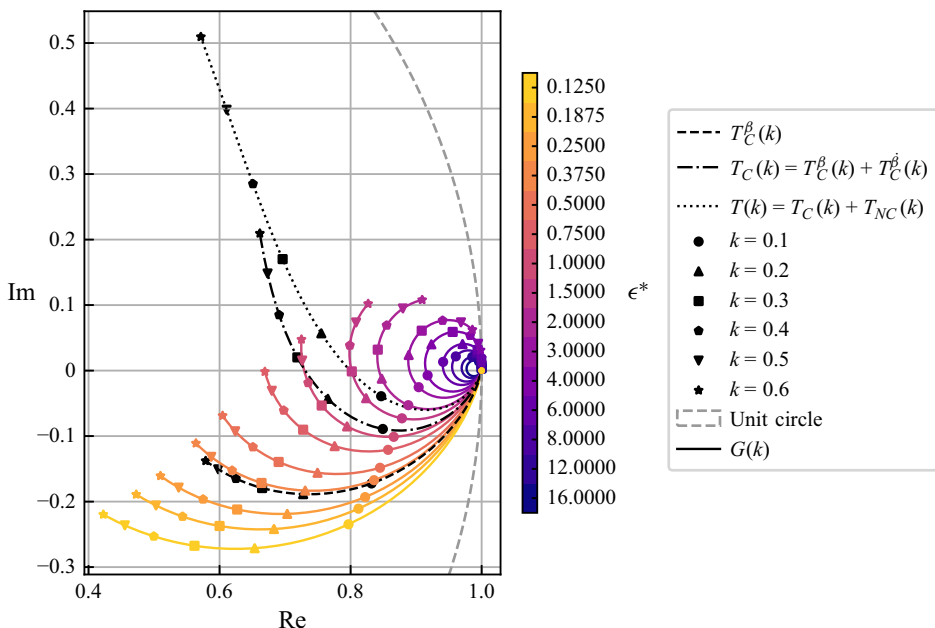


Figure 3. The closed-loop transfer function,  $G(k)$ , for a pitching flat plate,  $(dC_L/d\alpha = 2\pi)$ , in the complex plane. The function is shown for fifteen different Gaussian kernel widths. The Theodorsen function,  $T_C^\beta(k) = C(k)$ , the circulatory component of Theodorsen's transfer function,  $T_C(k)$ , and Theodorsen's complete transfer function,  $T(k)$ , are shown for reference, where the aerofoil pitches around the quarter-chord point ( $a = -1/2$ ).

where  $a \in [-1, 1]$  (from leading to trailing edge) is the location of the rotation axis of the pitching motion, and the complex Theodorsen function  $C(k)$  is given by

$$C(k) = \frac{K_1(ik)}{K_0(ik) + K_1(ik)}. \quad (4.14)$$

Here,  $K_0$  and  $K_1$  denote modified Bessel functions of the second kind. The superscripts  $(\cdot)^\beta$ ,  $(\cdot)^{\dot{\beta}}$  and  $(\cdot)^{\ddot{\beta}}$  denote terms depending on the pitch angle, pitch rate and pitch acceleration, respectively. In the frequency domain, these dependencies translate to terms scaling proportionally to  $1$ ,  $k$  and  $k^2$ , respectively. The classical ALM, as it was proposed by Sørensen & Shen (2002) and as it is also used in this work, only models the  $T_C^\beta(k)$  term. The remaining three terms, which are proportional to either  $k$  or  $k^2$ , are not captured by the ALM. It follows that the derived transfer function  $G(k)$  is the equivalent of the Theodorsen function  $C(k)$  consistent with the mathematical formulation of the ALM.

The ALM (for  $\epsilon_* \in [0.125, 16.0]$ ) and Theodorsen frequency domain solutions are compared in the complex plane in figure 3 and as a Bode plot in figure 4 up to a reduced frequency of  $k = 0.6$ . The magnitude of the transfer function is always  $|G| \leq 1$ , whereas the phase can be both positive or negative depending on the considered kernel width and the reduced frequency. In general, it can be seen that smaller kernel widths lead to larger damping. The phase of  $G(k)$  (see figure 4b) first decreases with increasing  $k$  before a characteristic phase inversion point is approached where the phase switches from negative to positive. This phase inversion point occurs for larger  $k$  as the kernel width decreases. The magnitude  $|C|(k)$  closely follows  $|G|(k; \epsilon_* = 0.375)$  for  $k < 0.4$ . Adding the second circulatory term  $T_C^{\dot{\beta}}(k)$ , which is proportional to the pitch rate, shows that the circulatory

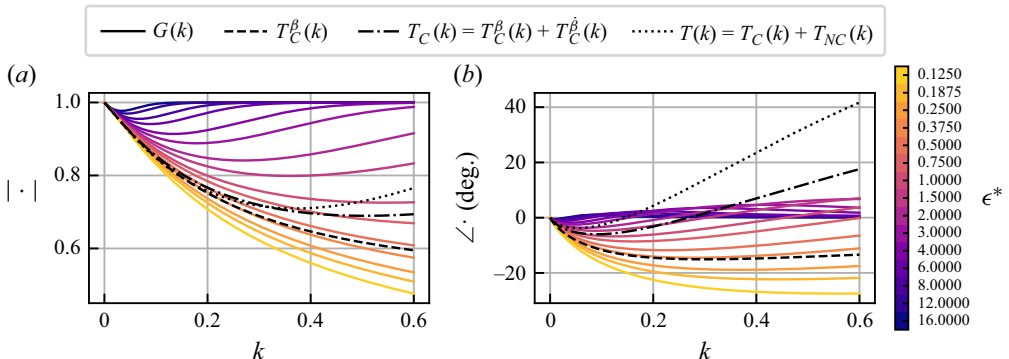


Figure 4. Magnitude (a) and phase (b) of  $G(k)$  for a pitching flat plate,  $(dC_L/d\alpha = 2\pi)$ , for fifteen different Gaussian kernel widths. The Theodorsen function,  $T_C^\beta(k) = C(k)$ , the circulatory component of Theodorsen's transfer function,  $T_C(k)$ , and Theodorsen's complete transfer function,  $T(k)$ , are shown for reference, where the aerofoil pitches around the quarter-chord point ( $a = -1/2$ ).

Theodorsen solution  $|T_C|(k)$  departs from  $|G|(k; \epsilon_* = 0.375)$  for  $k > 0.2$ . Finally, also adding the two non-circulatory terms leads to an additional deviation between the ALM and the complete Theodorsen solution  $|T|(k)$  for  $k > 0.4$ . The phase  $\angle C(k)$  closely follows  $\angle G(k; \epsilon_* = 0.375)$  for  $k < 0.4$ . In contrast to the magnitude, adding the second circulatory and eventually the two non-circulatory terms both leads to immediate deviations in phase compared with  $\angle G(k; \epsilon_* = 0.375)$  for any  $k$  rather than the two distinct points of departure of  $k = 0.2$  and  $k = 0.4$  observed for the magnitude.

These results suggest that when taking Theodorsen theory as a reference, the classical ALM can capture the unsteady damping of the lift accurately up to a reduced frequency of  $k = 0.2$ , whereas errors in phase are immediately encountered as soon as  $k > 0$ . However, these phase errors are relatively small and at  $k = 0.2$  the difference in phase predicted by the ALM and the complete Theodorsen theory is  $T(k = 0.2) - G(k = 0.2) \approx 19^\circ$ . The model validation shown later in § 7 will further support these identified bounds of the ability of the ALM to capture unsteady aerodynamic effects. For the purpose of further elucidating in § 7 the impact of the ALM not capturing the terms  $T_C^\beta$ ,  $T_{NC}^\beta$  and  $T_{NC}^{\ddot{\beta}}$ , we also define the extended closed-loop transfer function  $G_{Ext}(k)$  for the ALM. The extended ALM transfer function incorporates the three missing terms compared with Theodorsen theory in an *ad-hoc* approach and then is defined accordingly as

$$G_{Ext}(k) = \frac{\Delta C_L^{us}(k)}{\Delta C_L^{qs}(k)} = \frac{[\pi ik + \pi ak^2] + \frac{dC_L}{d\alpha} G(k) \left[ 1 + ik \left( \frac{1}{2} - a \right) \right]}{\frac{dC_L}{d\alpha}}, \quad (4.15)$$

where  $G(k)$  effectively replaces the Theodorsen function  $C(k)$ . It should be stressed that the current comparison between Theodorsen theory and the ALM is based on the classical ALM relying on point velocity sampling. An integral velocity sampling approach as introduced by Churchfield *et al.* (2017) could influence the transfer function and should be explored in future work.

## 5. Verification: model versus ALM-LES

In the previous three sections we have derived a model for the unsteady loading on an aerofoil modelled as a two-dimensional Gaussian body force. In this section we verify this

Case acronym	Operating point $\beta^0$	Forcing $C_x$	Forcing $C_y$	Actuation type	Magnitude $\Delta\alpha$ (step)	Amplitude $\Delta\beta$ (periodic)	Frequency $k$ (periodic)
A0-Cx-S4	0°	Yes	No	Step	4°	—	—
A0-Cxy-S4	0°	Yes	Yes	Step	4°	—	—
A8-Cx-S12	8°	Yes	No	Step	12°	—	—
A8-Cxy-S12	8°	Yes	Yes	Step	12°	—	—
A14-Cxy-S18	14°	Yes	Yes	Step	18°	—	—
A0-Cxy-P3-k01	0°	Yes	Yes	Step + periodic	4°	3°	$k = 0.1$
A0-Cxy-P3-k02	0°	Yes	Yes	Step + periodic	4°	3°	$k = 0.2$
A0-Cxy-P3-k03	0°	Yes	Yes	Step + periodic	4°	3°	$k = 0.3$
A0-Cxy-P3-k06	0°	Yes	Yes	Step + periodic	4°	3°	$k = 0.6$

Table 1. Overview of the investigated cases. The initial condition for all cases is  $\omega^{IC} = 0$ , corresponding to a situation without initial forcing. The step magnitude is defined as the difference between the pitch angle after the step (given by the operating point  $\beta^0$ ) and the angle of attack, which results in approximately zero lift force for the cambered aerofoil  $\Delta\alpha = \beta^0 - \alpha^{C_L=0}$  ( $\alpha^{C_L=0} \approx -4^\circ$ ). The periodic component of the actuation is of the form  $\beta(t_*) = \Delta\beta \sin(2kt_*)$ . The step components contain a continuous frequency spectrum where the magnitude of the Fourier transform of the step scales as  $|\hat{\beta}| \propto 1/k$ .

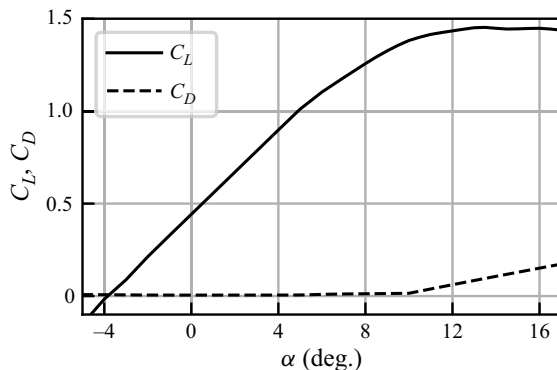


Figure 5. Tabulated lift,  $C_L(\alpha)$ , and drag,  $C_D(\alpha)$ , coefficients of the NACA64-A17 aerofoil.

model by comparing it with ALM-LES data to establish the bounds of its accuracy and model limitations.

### 5.1. Investigated cases

The range of investigated cases is chosen such that a range of operating points, types of actuation, reduced frequencies and the interplay between streamwise and normal forcing are explored. All cases are conducted using the NACA64-A17 aerofoil, which is, for example, also used for the outer part of the blade of the NREL 5 MW reference turbine (Jonkman *et al.* 2009). The aerofoil's tabulated lift and drag coefficients are shown in figure 5. Each investigated case is analysed for the set of Gaussian kernel widths  $\epsilon_* \in \{0.25, 0.5, 1.0, 2.0, 4.0\}$ . The lower limit is chosen here on the order of the steady-state optimal kernel width (Martínez-Tossas *et al.* 2017), while the upper limit corresponds to coarse grid ALM-LES simulations conducted for wind energy purposes. An overview of all cases and their acronyms is provided in table 1. In the following, the different cases are explained in more detail.

In order to characterise the obtained theoretical solutions and their scaling with the kernel width, we begin by considering two cases with a step in pitch angle. Both cases start from an initial condition of zero vorticity,  $\omega^{IC} = 0$ , i.e. zero forcing. This choice ensures that there is no mismatch between the initial conditions used for the model and LES. The simulation start thus corresponds to a sudden step actuation to reach the operating pitch angle  $\beta^0$  for  $t_* \geq 0$ . The considered operating points are  $\beta^0 = 0^\circ$  (A0-Cxy-S4) and  $\beta^0 = 8^\circ$  (A8-Cxy-S12). The same cases are also repeated without applying any normal forcing (A0-Cx-S4 and A8-Cx-S12). It should be noted that the frequency content of a step function is proportional to the inverse of the frequency ( $|\hat{\beta}| \propto 1/k$ ) and, thus, tests the model simultaneously across the entire frequency range. The step case A14-Cxy-S18 is only conducted for  $\epsilon_* = 0.25$  to obtain the largest forcing magnitudes. This case is used to perform a grid and domain size convergence study for the LES set-up.

The second set of cases considers the same initial step but additionally superposes continuous periodic pitch actuation with an amplitude of  $\Delta\beta = 3^\circ$  and reduced frequencies of  $k = 0.1$ ,  $k = 0.2$ ,  $k = 0.3$  and  $k = 0.6$  (indicated by the endings -k01, -k02, -k03 and -k06 of the case acronyms). The periodic pitch actuation is of the form  $\beta(t_*) = \Delta\beta \sin(2kt_*)$ . It is applied at the operating point  $\beta^0 = 0^\circ$  (A0-Cxy-P3-k...). This second set of cases is well suited to test the predictions of the derived closed-loop transfer function for an isolated frequency component after the initial transient decayed.

## 5.2. Employed numerical code and simulation set-up

Numerical nonlinear reference results for the assessment of the developed model are obtained by means of LES using the open-source code AMR-Wind (available at <https://github.com/Exawind/amr-wind>). The AMR-Wind code solves the three-dimensional incompressible Navier–Stokes equations on block-structured Cartesian grids and is specifically designed for wind energy applications. For details on the numerical schemes employed in AMR-Wind, the reader is referred to Almgren *et al.* (1998), Sharma *et al.* (2024) and Kuhn *et al.* (2025). For the purpose of verifying the developed model, which is based on the Euler equations, the governing equations are solved in the limit of infinite Reynolds number by setting the molecular viscosity to zero. Throughout the simulations, the inflow and the wake flow behind the actuator points remain laminar, removing the need for explicit turbulence modelling.

This work utilises AMR-Wind's implementation of the ALM for straight translating wings. The AMR-Wind code does not allow for strictly two-dimensional simulations; rather, we simulate the aerofoil in a three-dimensional domain as an infinite wing, i.e. periodic boundary conditions are imposed in the spanwise direction. The lower and upper boundary condition in the normal direction is a slip wall ( $y$ -direction). In the streamwise direction ( $x$  direction), a constant inflow velocity of  $\mathbf{u} = U_\infty \mathbf{i}$  is imposed at the upstream boundary (which in non-dimensional units corresponds to  $\mathbf{u}_* = \mathbf{i}$ ), and a pressure outflow boundary condition is applied at the downstream boundary. The wing spans two actuator points located on the spanwise boundaries of the domain at which the actuator forces are applied. The forces are regularised with a two-dimensional isotropic Gaussian kernel of width  $\epsilon_*$ . The velocity used for the actuator force calculation is the known inflow velocity (see Appendix C).

The convergence of LES results with domain size and grid resolution is studied in Appendix D for the A14-Cxy-S18 case using  $\epsilon_* = 0.25$ . Based on this convergence study, all simulations are conducted with a semi-domain height  $L_{y_*} = 256$  and an upstream fetch of  $L_{x_*}^{upstr} = 256$  between the inflow boundary and the actuator point. The streamwise distance from the actuator point to the outlet is  $L_{x_*}^{downstr} = T_* + L_{y_*}$ , where  $T_*$  is the

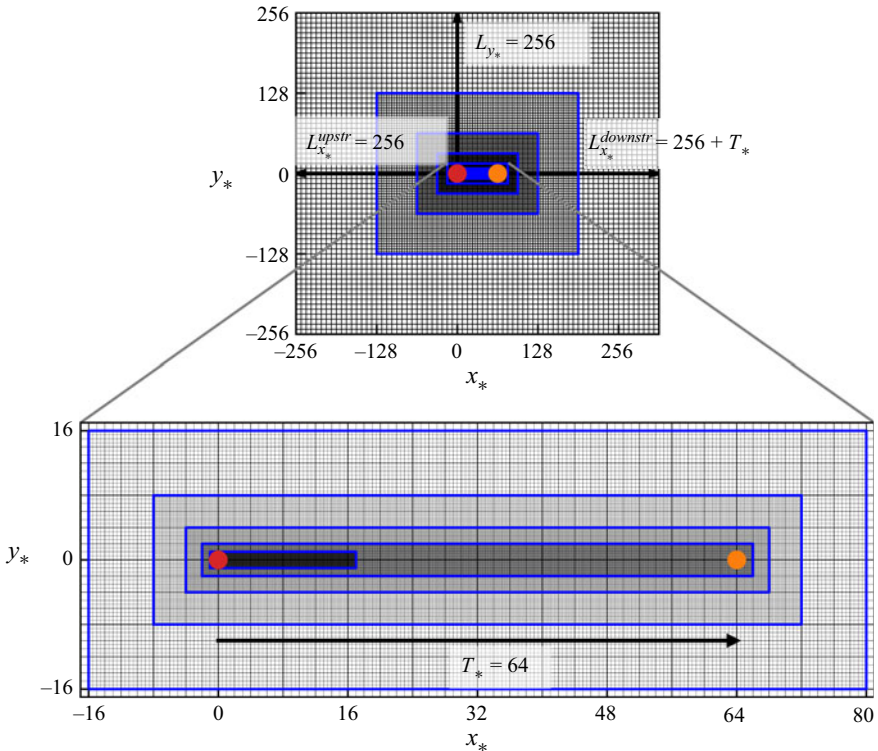


Figure 6. The LES domain and grid refinement structure for the Gaussian kernel width  $\epsilon_* = 0.25$  with the resolution on the finest grid level being  $\epsilon_*/\Delta x = 8$ . Note that the domain here is configured for a simulation time of  $T_* = 64$  in order to keep the aspect ratio limited for visual clarity. The actual simulations are performed for  $T_* = 128$  (steps) and  $T_* = 256$  (periodic). The red dot marks the actuator point. The orange dot marks the approximate downstream location of the start-up vortex at time  $t_* = T_*$ .

maximum simulated time. The grid resolution on the coarsest grid level is constant for all simulations; however, depending on the studied kernel width, four ( $\epsilon_* = 4$ ) to eight ( $\epsilon_* = 0.25$ ) refinement levels are added such that on the finest grid around the actuator point the resolution is always  $\epsilon_*/\Delta x_* = 8$ . The grid resolution between two adjacent grid levels varies with a constant factor of 2. The size of the finest grid level is dependent on the kernel width. Its extent in the  $x$  and  $y$  directions is  $-4\epsilon_* < x_* < 16 + 4\epsilon_*$  and  $-4\epsilon_* < y_* < 4\epsilon_*$ , respectively. Letting the index  $m$  denote the grid level (the finest being  $m = 0$ ), the extent of all other refinement levels ( $m > 0$ ) in  $x$  and  $y$  is given by  $-4\epsilon_* 2^m < x_* < T_* + 4\epsilon_* 2^m$  and  $-4\epsilon_* 2^m < y_* < 4\epsilon_* 2^m$ . The time-step size  $\Delta t_{*,LES}$  is chosen such that the Courant–Friedrichs–Levy (CFL) number defined on the finest grid level is  $CFL < 0.5$  at all times. Step cases are simulated up to  $T_* = 128$ , whereas the step cases followed by periodic actuation are simulated up to  $T_* = 256$ . These long simulation times provide enough time for the actuator loading to reach the new steady state (step cases) or periodic limit cycle (step plus periodic cases) after the decay of the initial transient. The simulation time-dependent streamwise domain length ensures that no vorticity is truncated at the outlet. The simulation time for the periodic cases is chosen twice as long in order to collect a large number of actuation periods, even for the smallest frequency  $k = 0.1$ . The LES set-up is visualised in figure 6.

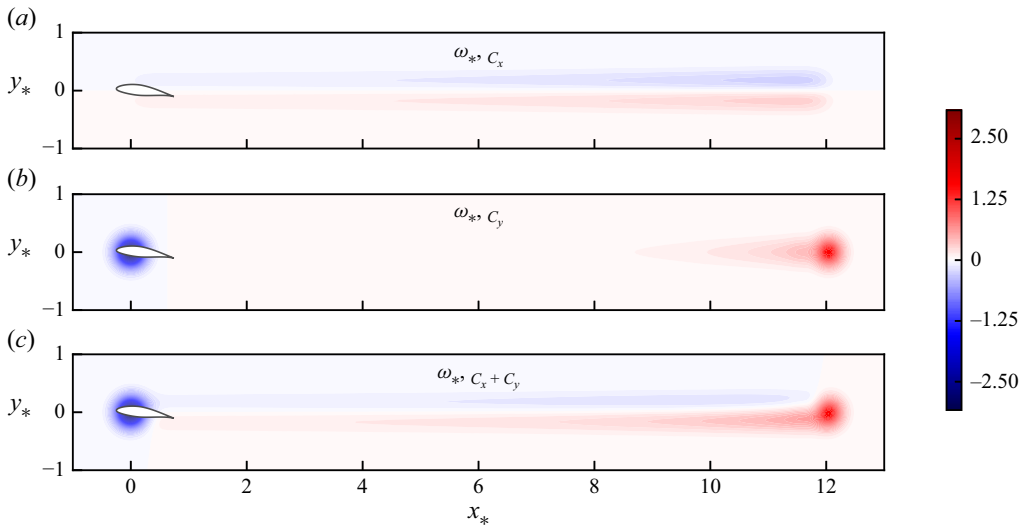


Figure 7. Model solution for the vorticity field of the A8-Cxy-S12 case with the kernel width  $\epsilon_* = 0.25$  at time instance  $t_* = 12$ . The vorticity created by streamwise  $C_x$  and normal  $C_y$  forcing is shown in (a) and (b), respectively. The total resultant vorticity field is shown in (c). The aerofoil modelled by the Gaussian body force is shown in white with a black outline. The aerofoil's quarter-chord point is located at the actuator point  $(x_*^{Act}, y_*^{Act})^\top = (0, 0)^\top$ .

### 5.3. Response to pitch step actuation

We start by probing the developed model for two pitch step actuation cases within the linear regime of the lift curve. Their respective operating points are  $\beta^0 = 0^\circ$  (A0-Cxy-S4) and  $\beta^0 = 8^\circ$  (A8-Cxy-S12). The initial condition is chosen as undisturbed free-stream flow, i.e. no forcing is active. Consequently, the two operating points correspond to effective angle of attack steps of  $\Delta\alpha = 4^\circ$  and  $\Delta\alpha = 12^\circ$  upon simulation start (the lift coefficient of the cambered aerofoil is approximately zero at  $\alpha \approx -4^\circ$ ).

The vorticity distribution around the aerofoil and in the wake as predicted by the model (see Appendix B) with  $\epsilon_* = 0.25$  is shown in figure 7 for the larger pitch step case A8-Cxy-S12. Around the aerofoil, a bound vortex forms in response to the non-zero loading after  $t_* > 0$ . The bound vortex is accompanied by the formation of a start-up vortex, which ensures conservation of the overall vorticity. Since the model assumes the advection speed in the wake to match the free-stream velocity, the start-up vortex is located at  $x_* = 12$  in the wake at the shown time instance  $t_* = 12$ . Furthermore, it is seen that the wake centreline  $(x_*, y_* = 0)^\top$  is the symmetry axis for both the vorticity due to streamwise and the vorticity due to normal forcing (figure 7a,b). The vorticity due to streamwise forcing exhibits an anti-symmetric distribution around this symmetry axis, whereas the normal forcing contribution is distributed symmetrically around the wake centreline. These distributions stem from the symmetry properties of the forcing terms in the linearised vorticity transport equation (2.3).

The formation of the start-up vortex and its subsequent advection downstream causes a dynamic angle of attack response. A comparison of the model and the LES solution for this response is shown in figure 8 for the small pitch step case A0-Cxy-S4. The start-up vortex induces velocity at the actuator point, which in turn alters the angle of attack. As it is advected further downstream, its influence on the angle of attack fades, which leads the angle of attack to converge towards the new steady-state operating point  $\alpha = \beta^0 = 0^\circ$ .

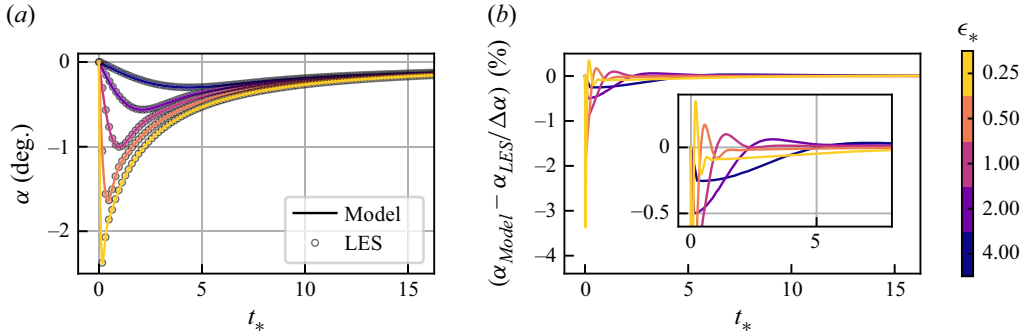


Figure 8. Comparison of the model solution and LES reference for the initial time evolution of the angle of attack (a) and the corresponding relative error (b) for the pitch step actuation case A0-Cxy-S4. Reference data points are only shown in steps of  $4\Delta t_{*,\text{LES}}/\epsilon_*$ .

(figure 8a). The initial modulation of the angle of attack depends on the kernel width since it sets the local strength of the applied forcing and, thus, also the strength of the start-up vortex. Furthermore, the core size of the start-up vortex is also set by the kernel width. The core size determines the time period between  $t_* = 0$  and the time instance when the angle of attack reaches its minimum. The minimum angle of attack is attained faster with a smaller kernel width and, thus, core size.

The model error compared with the LES reference is presented in figure 8(b). The very initial relative angle of attack error is as large as 3.4 % and then subsequently drops to the order of tenths of a percent. The relative error starts approaching zero after the actuator point no longer lies within the vortex core region of the start-up vortex. The relative error is larger for smaller kernel widths as long as there is overlap between the vortex core and the actuator point. This is the case because the velocity induced by the bound and start-up vortex both reach their absolute maximum values in proximity to their respective core boundary, where the maximum values increase with decreasing kernel width. Thus, after the time instance  $t_* > |x_*^{\text{Act}} - t_*| \approx |0 - \epsilon_*| = \epsilon_*$  the impact of the bound vortex on the trajectory of the start-up vortex as well as the impact of the start-up vortex on the angle of attack at the actuator point start to decrease. Hence, the effect of modelling errors also decreases as soon as  $t_* \approx \epsilon_*$ . The larger pitch step case A8-Cxy-S12 shown in figure 9 follows the previous observations made apart from the relative error evolution for  $\epsilon_* = 0.25$ . In this case, the error also persists after the vortex core no longer overlaps with the actuator point and only fades at  $t_* \approx 10$ . The larger pitch step combined with the smallest kernel width makes for a stronger bound vortex, increasingly challenging the model, which is based on a linearisation around the vorticity-free background flow. The detailed impact of the error due to the linearisation will be explored in the following § 6.

We explore the two pitch step cases further by turning our attention towards the loading, which the model ultimately should predict. The model is able to accurately reproduce the time evolution of the streamwise,  $C_x$ , and normal,  $C_y$ , force coefficients for both the small (figure 10b,d) and large (figure 11b,d) pitch step cases. In particular, the transient drop in normal forcing and peak in streamwise forcing caused by the start-up vortex are captured. It is also worthwhile to study the induced velocities at the actuator point, which induce the change in flow angle and, thus, angle of attack (panels *a* and *c* of figures 10 and 11). The model matches the LES prediction for the normal induced velocity,  $v_*$ , for both pitch step magnitudes, but discrepancies are apparent for the streamwise induced velocity,  $u_*$ , which become more pronounced for smaller kernel widths and the larger pitch step (compare figures 10*a* and 11*a*). This discrepancy also matches the previous

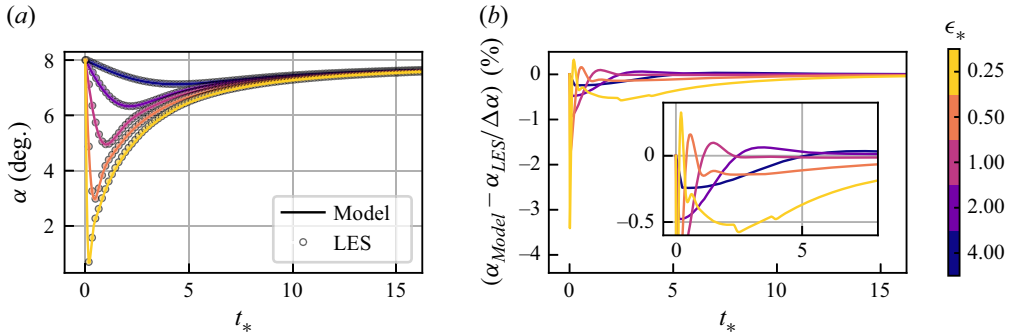


Figure 9. Comparison of the model solution and LES reference for the initial time evolution of the angle of attack (a) and the corresponding relative error (b) for the pitch step actuation case A8-Cxy-S12. Reference data points are only shown in steps of  $4\Delta t_{*,LES}/\epsilon_*$ .

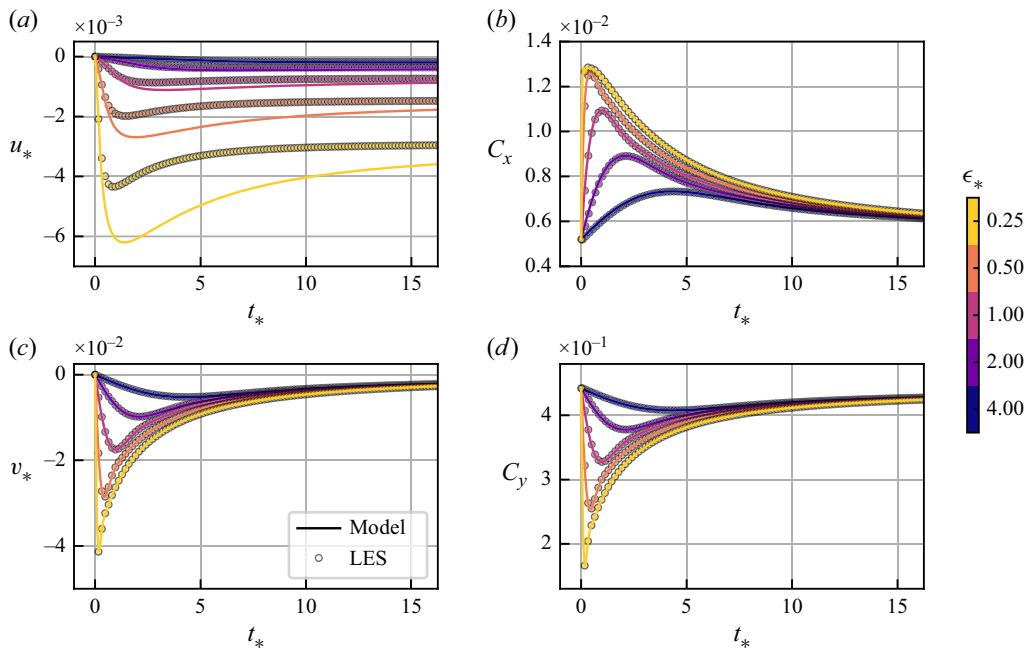


Figure 10. Comparison of the model solution and LES reference for the initial time evolution of the streamwise (a) and normal (c) induced velocity and the streamwise (b) and normal (d) force coefficients for the pitch step actuation case A0-Cxy-S4. Reference data points are only shown in steps of  $4\Delta t_{*,LES}/\epsilon_*$ .

observation that the angle of attack error of the A8-Cxy-S12 case for  $\epsilon_* = 0.25$  persists for a longer time. Since we deal with small perturbation velocities, the flow angle is small and, thus, approximately given by  $\phi \approx v_*$ . Thus, the error in streamwise induced velocity does not affect the quality of the streamwise and normal force coefficients as long as the small perturbation assumption is justified. In fact,  $u_*$  is a measure of the system's nonlinearity and is relevant for the flow angle calculation given larger induced velocities. However, larger induced velocities start to challenge the linearisation of the vorticity transport equation for the model derivation. Thus, the mismatch for  $u_*$  and its increase for stronger forcing is consistent. In § 6 we show that the observed streamwise velocity

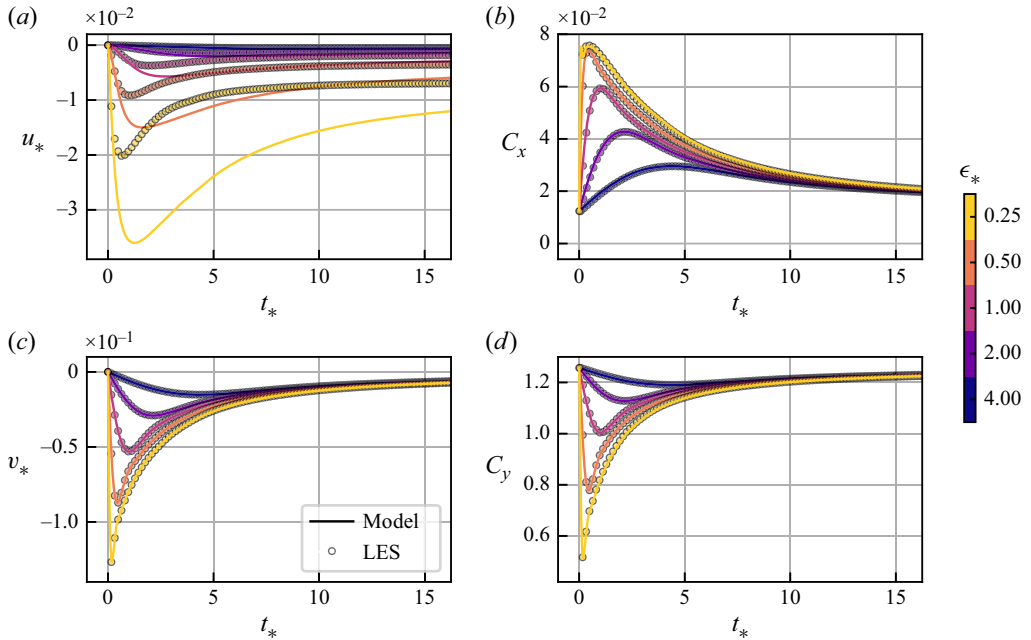


Figure 11. Comparison of the model solution and LES reference for the initial time evolution of the streamwise (a) and normal (c) induced velocity and the streamwise (b) and normal (d) force coefficients for the pitch step actuation case A8-Cxy-S12. Reference data points are only shown in steps of  $4\Delta t_{*,LES}/\epsilon_*$ .

residual is explained by the vorticity residual obtained from the difference of the model (linear) and the LES reference (nonlinear) solution. However, the two pitch step cases show that the developed model can predict the loading on the aerofoil in the linear regime of the lift curve despite the mismatch in  $u_*$ . The cases also illustrate the importance of the kernel width. The largest studied kernel width of  $\epsilon_* = 4.0$  barely modifies the normal force coefficient, while the kernel width  $\epsilon_* = 0.25$ , which is of the order of the steady-state optimal value, results in a transient drop of more than 50 % (see figure 11d).

Motivated by the mismatch of the streamwise induced velocity, we also conduct the pitch step cases with an absent normal force  $C_y = 0$  (the cases labelled A0-Cx-S4 and A8-Cx-S12). The resulting evolution of  $u_*$  and the corresponding absolute model error are shown in figure 12 for the large pitch step case. In the absence of normal forcing, the previously observed mismatch between the model and the LES reference vanishes, and the model error after the initial time steps is 2 orders of magnitude smaller than  $u_*$ . This highlights the impact of the assumptions made when linearising the vorticity transport equation for the model derivation. Neglecting the nonlinear transport terms, which include the induced velocity, causes the model to miss the normal displacement of the start-up vortex as it is advected in the induced normal velocity field of the bound vortex, which is maximal at the wake centreline ( $x_*, y_* = 0$ ). This lack of vertical displacement is also apparent in the previously shown model solution for the vorticity field (figure 7). Switching off the normal forcing,  $C_y$ , removes its anti-symmetric contribution to the induced velocity field. Thus, as long as the streamwise induced velocity remains small, the model can now correctly predict  $u_*$  too. It can also be noted that the induced streamwise velocity after the decay of the transient tends towards the steady-state limit given by  $u_* = -C_x/(4\sqrt{\pi}\epsilon_*)$ , which was also derived by Martínez-Tossas *et al.* (2017).

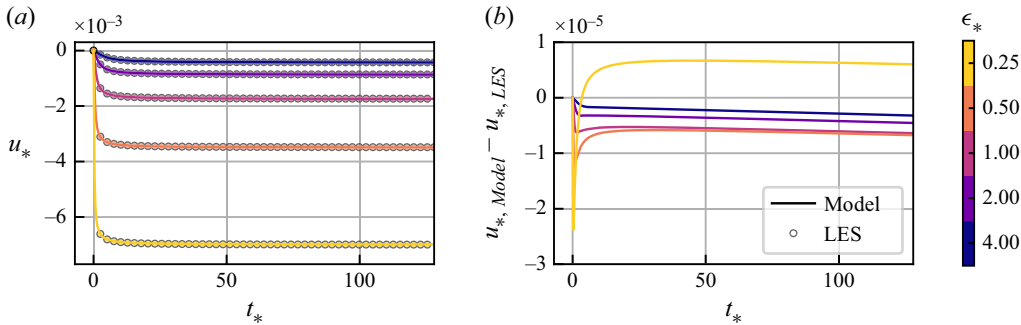


Figure 12. Comparison of the model solution and LES reference for the time evolution of the streamwise induced velocity (a) and the corresponding absolute error (b) for the pitch step actuation case A8-Cx-S12. Reference data points are only shown in steps of  $64\Delta t_{*,\text{LES}}/\epsilon_*$ .

#### 5.4. Response to periodic pitch actuation

After characterising the developed model with pitch steps, we now move on towards signals that are more present in reality, i.e. smooth signals and, in particular, periodic signals with sinusoidal shape. The solution to the latter can also be used to construct the solution for more complex forcing signals via their representation in terms of a Fourier series. In the following, we consider the four cases A0-Cxy-P3-k01, A0-Cxy-P3-k02, A0-Cxy-P3-k03 and A0-Cxy-P3-k06, which initially possess the same pitch step as the A0-Cxy-S4 case but then proceed with a continuous sinusoidal pitch actuation of amplitude  $\Delta\beta = 3^\circ$ . The four different cases vary in terms of the actuation frequency; namely, the four reduced frequencies  $k = 0.1, k = 0.2, k = 0.3$  and  $k = 0.6$  are considered.

Representative angle of attack evolutions obtained for these four reduced frequencies are shown for the case of  $k = 0.3$  in figure 13. The angle of attack now varies periodically, where its initial evolution shows a transient due to the influence of the start-up vortex, which initially is still present. After the transient, the angle of attack attains a limit cycle. For reference, figure 13 shows horizontal lines indicating the angle of attack amplitude predicted by the model closed-loop transfer function (given by  $|G(k)|\Delta\beta$ ). The frequency domain solution in terms of the transfer function is able to predict the limit cycle amplitude modulation since the peaks of the angle of attack time series converge towards the horizontal lines. Therefore, the effect of increasingly smaller kernel widths is a successive reduction of the angle of attack amplitude compared with the quasi-steady reference ( $\Delta\beta = 3^\circ$ ) and a successive increase in phase lag. For the given aerofoil and reduced frequency of  $k = 0.3$ , the reduction in effective angle of attack amplitude is as large as 35 % for the smallest studied kernel width  $\epsilon_* = 0.25$ , which is of the order of the steady-state optimal kernel width. The evolution of the induced velocities and the force coefficients corresponding to the previous angle of attack evolution of the A0-Cxy-P3-k03 case are shown in figure 14. Similar to the step cases, the model cannot predict the correct streamwise induced velocity,  $u_*$ , in the presence of combined streamwise and normal forcing, where the error increases with decreasing kernel width.

After the decay of the initial transient, it is convenient to represent the force coefficients in terms of hysteresis plots (figure 15). The grey reference lines in this plot show the quasi-steady force coefficients, i.e. the forcing as it would be obtained when the instantaneous angle of attack matches the instantaneous pitch angle. However, the velocity induced by the shed vorticity in the wake causes a non-zero flow angle, and it is  $\alpha \neq \beta$ , which causes the unsteady force coefficients to differ from the quasi-steady ones both in terms

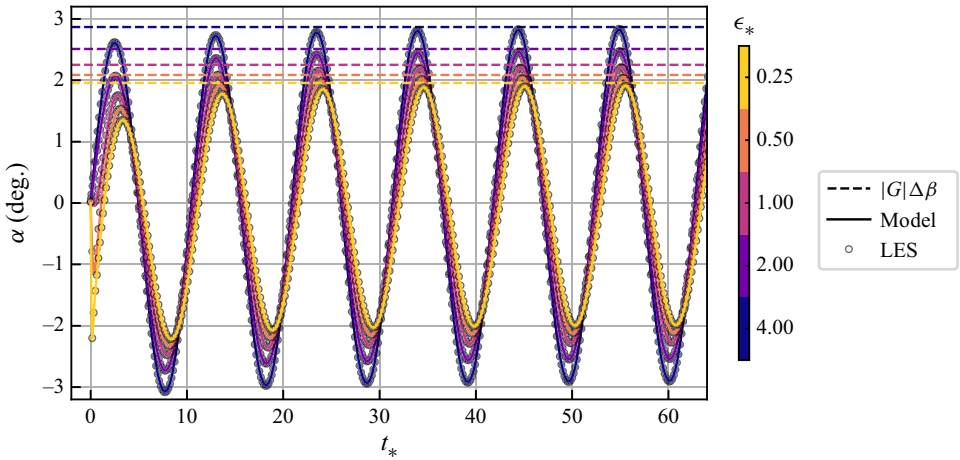


Figure 13. Comparison of the model solution and LES reference for the initial time evolution of the angle of attack for the periodic pitch actuation case A0-Cxy-P3-k03. Reference data points are only shown in steps of  $4\Delta t_{*,LES}/\epsilon_*$ . The horizontal coloured dashed lines indicate the unsteady angle of attack amplitudes  $|G(k)|\Delta\beta$  predicted by the model closed-loop transfer function  $G(k)$ .

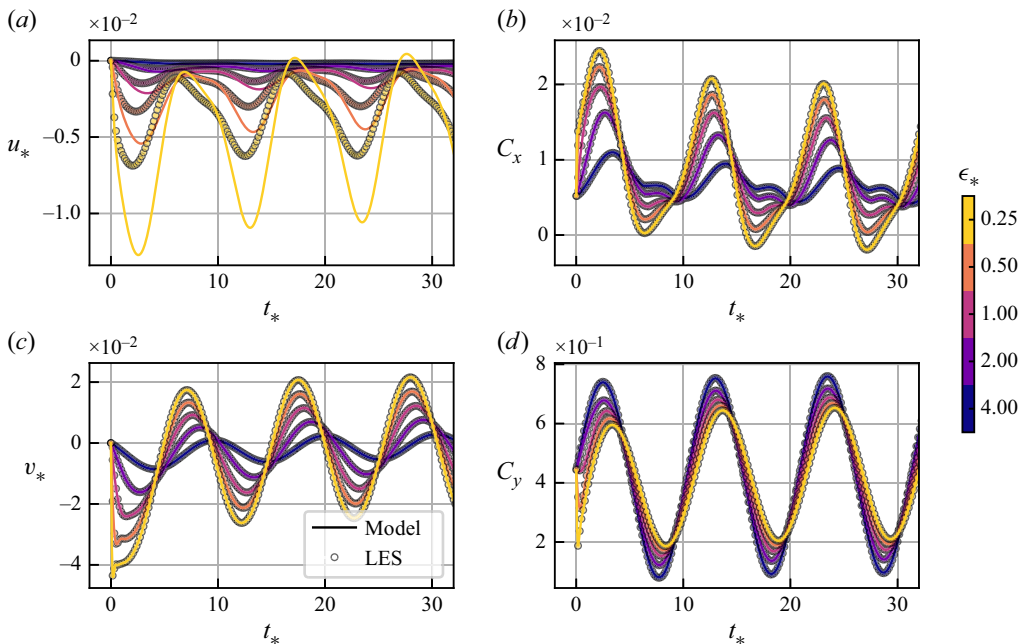


Figure 14. Comparison of the model solution and LES reference for the initial time evolution of the streamwise (a) and normal (c) induced velocity and the streamwise (b) and normal (d) force coefficients for the periodic pitch actuation case A0-Cxy-P3-k03. Reference data points are only shown in steps of  $4\Delta t_{*,LES}/\epsilon_*$ .

of magnitude and phase. These differences between unsteady and quasi-steady force coefficients depend on the kernel width. For the shown case of  $k = 0.3$  in figure 15(b), it can be seen that smaller kernel widths cause stronger hysteresis, e.g. the minor axis of the ellipse for  $C_y$  is larger (phase modulation). Furthermore, the major axis of the

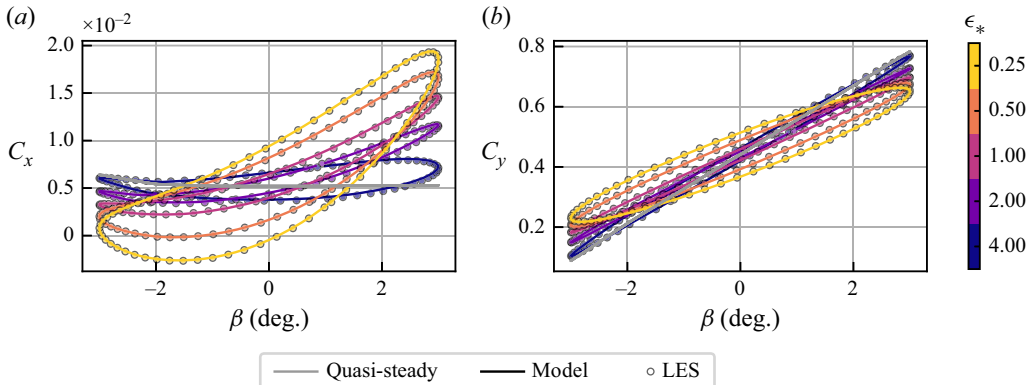


Figure 15. Comparison of the model solution and LES reference for the hysteresis of the streamwise (a) and normal (b) force coefficient (periodic pitch actuation case A0-Cxy-P3-k03). The quasi-steady references  $C_x(\beta)$  and  $C_y(\beta)$  are shown in grey.

ellipse becomes increasingly tilted towards the horizontal axis, i.e. the force amplitude is damped compared with the quasi-steady case (amplitude modulation). For the streamwise forcing,  $C_x$ , smaller kernel widths also lead to more pronounced hysteresis as observed for  $C_y$  (figure 15a). However, the trend for the amplitude modulation is different compared with  $C_y$  in the sense that the unsteady solution for  $C_x$ , compared with the quasi-steady reference, shows an increase in amplitude rather than a decrease. This amplitude increase is larger for smaller kernel widths because for these cases, the normal induced velocity reaches larger values (figure 14c), and thus, the same follows for the flow angle  $\phi$ . Since the streamwise force coefficient in the linear regime of the lift curve is dominated by the  $C_L$  contribution, it attains its maximum when the product  $-C_L(\alpha) \sin(\phi)$  becomes maximal, which in addition to large  $C_L$  also requires flow angles close to their maximal negative value since  $C_L$  and  $v_*$  are approximately half a period out of phase (compare panels c and d of figure 14).

Given the dominance of the normal forcing in the linear regime of the lift curve for which the present model is developed, the observations regarding the phase and amplitude modulations made from the time series and hysteresis curves can be concisely summarised in a Bode plot. Figure 16(a,b) shows the Bode magnitude and Bode phase plot of the model closed-loop transfer function  $G(k)$ , which was derived assuming that  $C_D = 0$ . Here  $G(k)$  is computed using the linearised value of the lift slope of the NACA64-A17 aerofoil at the operating point  $\beta^0 = 0^\circ$ , matching the operating point of the periodic actuation cases. The model solution is presented for the set of kernel widths  $\epsilon_* \in \{0.25, 0.5, 1.0, 2.0, 4.0\}$  in the range  $k \in [0, 0.75]$ . In addition, the phase and amplitude modulation are extracted from the last period of the LES reference data for the cases A0-Cxy-P3-k01 ( $k = 0.1$ ), A0-Cxy-P3-k02 ( $k = 0.2$ ), A0-Cxy-P3-k03 ( $k = 0.3$ ) and A0-Cxy-P3-k06 ( $k = 0.6$ ), which are shown as dots in the plot. The transfer function solution matches the LES reference for all four reduced frequencies.

For reduced frequencies  $k \leq 0.3$ , magnitude and phase trends are monotone for varying kernel widths at a given constant frequency. However, the magnitude and phase variation with frequency for a constant kernel width are not monotone. The magnitude reaches a minimum, after which it again approaches  $|G| = 1$  for further increasing  $k$ . The convergence to  $|G| = 1$  happens for smaller  $k$ , the larger the kernel width, and for the shown relevant frequency range, it is only visible for  $\epsilon_* = 4.0$ . In this limit, the unsteady lift magnitude again approaches the quasi-steady solution. Also, the phase tends towards a

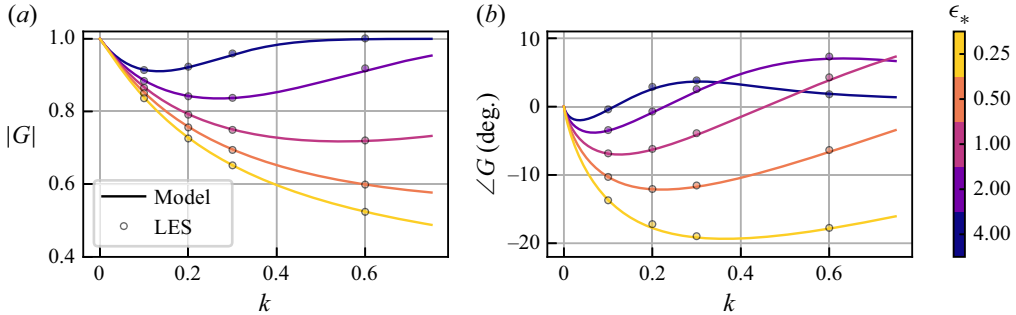


Figure 16. The magnitude (a) and phase (b) of the model closed-loop transfer function  $G(k)$  for the NACA64-A17 aerofoil at the linearisation point  $\beta^0 = 0^\circ$ . Dots indicate the corresponding amplitude and phase modulations extracted from the last period of the LES reference cases A0-Cxy-P3-k01, A0-Cxy-P3-k02, A0-Cxy-P3-k03 and Cxy-P3-k06.

common limit of  $\angle G = 0^\circ$  for all kernel widths as  $k \rightarrow \infty$ , although this convergence happens for  $k > 0.75$  except for the largest studied kernel width. Consequently, for a chosen kernel width representing the aerofoil, the maximum reduction of the quasi-steady lift amplitude  $\min(|G(k; \epsilon_*)|)$  and maximum phase lag  $\min(\angle G(k; \epsilon_*))$  occur for an intermediate reduced frequency  $0 < k < \infty$ . Furthermore, the maximum phase lag occurs for smaller  $k$  than does the maximum amplitude reduction. Within the range of relevant  $k$ , smaller kernel widths lead to larger damping. Comparing  $\epsilon_* = 0.25$ , which is of the order of the steady-state optimal kernel width, with  $\epsilon_* = 4$ , which corresponds to a value encountered for coarse grid ALM-LES for wind energy purposes, one would miss about  $\Delta(|G|) \approx 0.3$  of damping and  $\Delta(\angle G) \approx 23^\circ$  of phase lag at a reduced frequency of  $k = 0.3$ . This difference is the unsteady equivalent of the steady-state lift error observed for suboptimal large kernel widths, which motivated the development of smearing corrections (Martínez-Tossas & Meneveau 2019; Meyer Forsting *et al.* 2019a; Dağ & Sørensen 2020; Kleine *et al.* 2023a).

The source of the unsteady error due to large kernel widths can also be made apparent by comparing the topology of the shed vorticity in the wake for varying  $\epsilon_*$  (figure 17). The regularisation with the Gaussian kernel conserves both the integrated force as well as the integrated vorticity. That is assuming the magnitude of the point force would not be affected by the induced velocities, which in reality it is. But even neglecting this effect, the conservation on an integral level can still be achieved by locally very different vorticity distributions. The vorticity for small kernel widths is more localised, and thus, integral conservation directly implies locally higher vorticity magnitudes in proximity of the aerofoil and the wake centreline. In turn, large kernel widths spread the vorticity across a larger area, reducing its local magnitude. Since the induced velocity scales with the inverse of the distance outside of the vortex core, this directly implies smaller induced velocities at the actuator point. Finally, the phase error is also apparent from the vorticity distributions. To this end, one can track the vertical band of zero vorticity, which is located between the bound vortex (blue) and the neighbouring positive vorticity patch (red) directly downstream of the aerofoil. Its location is closest to the aerofoil for  $\epsilon_* = 0.25$  and then shifts continuously farther downstream for larger kernel widths, i.e. the larger the kernel width, the further ahead the phase.

Summarising the model verification presented in this section, we conclude that the developed model matches the ALM-LES predictions for the unsteady loading on the aerofoil within the considered operating regime, which is the linear part of the lift curve.

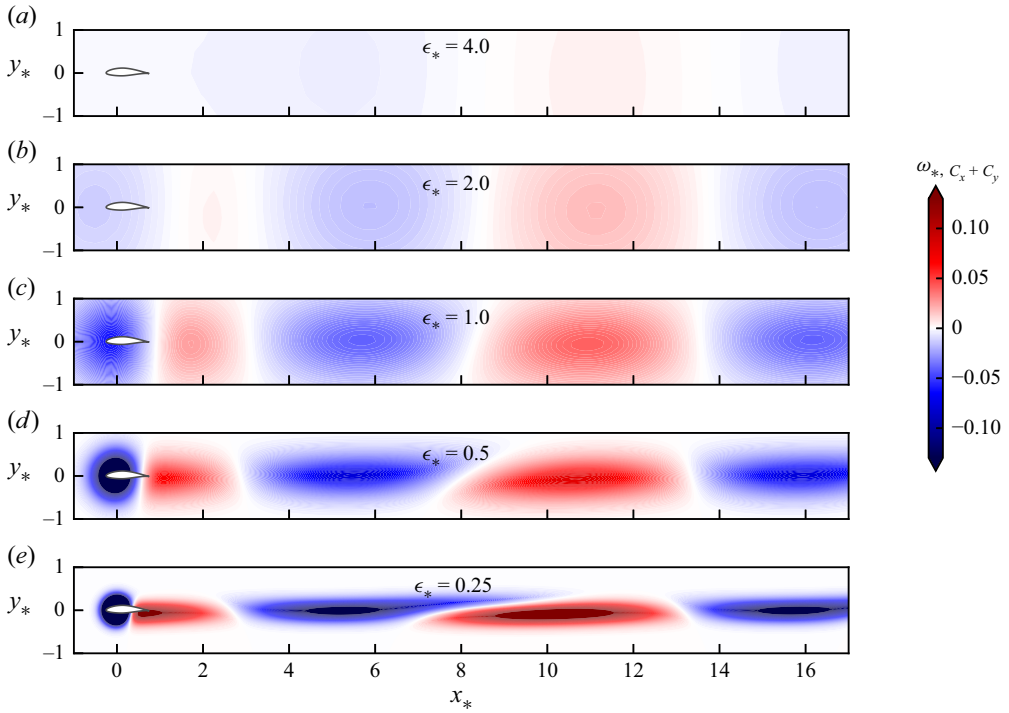


Figure 17. Model solution for the total resultant vorticity field of the A0-Cxy-P3-k03 case at time instance  $t_* = 32$ . Panels (a–e) show the solution for the Gaussian kernel widths  $\epsilon \in \{4.0, 2.0, 1.0, 0.5, 0.25\}$ . The aerofoil modelled by the Gaussian body force is shown in white with a black outline. The aerofoil's quarter-chord point is located at the actuator point  $(x_*^{\text{Act}}, y_*^{\text{Act}})^T = (0, 0)^T$ .

The step and periodic actuation cases demonstrated the frequency-dependent impact of the Gaussian kernel width on the unsteady loading, both in terms of lift reduction and added phase lag.

## 6. Discussion: assessing the model error with respect to LES-ALM

The preceding verification results show that within the linear regime of the lift curve, the derived model solutions match the ALM-LES predictions of the unsteady loading on the aerofoil. However, it also became clear that even within this regime, the model cannot reproduce the correct streamwise induced velocity in the presence of combined forcing in the streamwise and normal directions. This deficiency does not affect the accuracy of the results as long as the small-angle approximation for the flow angle is valid. Nevertheless, due to this observation we already pointed in § 5.3 towards the fact that there is a coupling between the two forcing directions, which is neglected for the derivations in this work. We derive here the exact form of the neglected terms and assess their magnitude and spatial localisation with respect to the reference LES data.

The vorticity transport equation for the two-dimensional problem was introduced in (2.2) and reads in expanded form as

$$\frac{\partial \omega_*}{\partial t_*} + \frac{\partial \omega_*}{\partial x_*} + u_* \frac{\partial \omega_*}{\partial x_*} + v_* \frac{\partial \omega_*}{\partial y_*} = \underbrace{\frac{-y_* C_x + x_* C_y}{\pi \epsilon_*^4} e^{-(x_*^2 + y_*^2)/\epsilon_*^2}}_{\mathcal{N}(u_*, \omega_*)} \underbrace{F(x_*, y_*, t_*)}_{(6.1)}$$

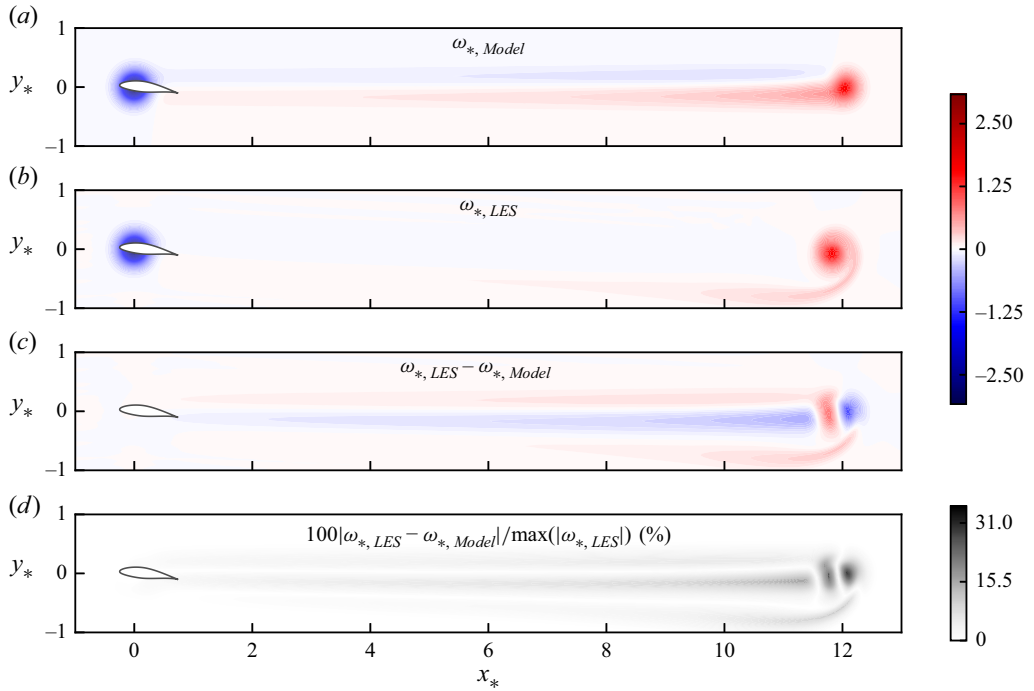


Figure 18. Model (a) and LES (b) solution for the total vorticity field of the A8-Cxy-S12 case for  $\epsilon_* = 0.25$  at time instance  $t_* = 12$ . The difference between the model and LES solution is shown in (c). The relative error is shown in (d) where the reference for the normalisation of the error is the maximum value of the absolute vorticity in the  $x_*$  –  $y_*$  plane. The aerofoil modelled by the Gaussian body force is shown with a black outline. The aerofoil’s quarter-chord point is located at the actuator point  $(x_*^{Act}, y_*^{Act})^\top = (0, 0)^\top$ .

In order to arrive at the final linearised equation(2.3) as introduced in § 2, we need to assume that the nonlinear term  $\mathcal{N}(\mathbf{u}_*, \omega_*)$  can be neglected, which means that if the other remaining terms are all of order  $\mathcal{O}(1)$ , the nonlinear term should be at maximum of order  $\mathcal{N} = \mathcal{O}(1/10)$ . An increasing magnitude of the forcing  $F(x_*, y_*, t_*)$  increasingly challenges this linearisation. Analysis of the forcing shows that it is locally linearly proportional to the magnitude of the force coefficients  $F \propto C_i$  ( $i \in x, y$ ), but inversely proportional to the fourth power of the kernel width  $F \propto 1/\epsilon_*^4$ . However, in addition to the Gaussian contribution, the forcing term attains a maximum value of  $\max(x_* \exp(-x_*^2/\epsilon_*^2)) \approx 0.43\epsilon_*$  at  $x = \epsilon_*/\sqrt{2}$ . Neglecting the effect of the kernel on the strength of the forcing via the induced velocity, this scaling shows that within the linear region of the lift curve, doubling the angle of attack only doubles the local forcing magnitude, whereas halving the Gaussian kernel width leads to an eightfold increase in local forcing (i.e.  $F \propto 1/\epsilon_*^3$ ).

Based on this scaling analysis, we focus the error analysis on the smallest kernel width of  $\epsilon_* = 0.25$ . Figure 18(a,b) shows the vorticity solution for the large pitch step case A8-Cxy-S12 obtained both from the model and the LES at time instance  $t_* = 12$ . The LES that solves for all terms present in (6.1) predicts a roll-up and normal displacement of the start-up vortex. Furthermore, the nonlinear terms break the (anti-) symmetric vorticity distribution of the model with respect to the wake centreline. In contrast, the model cannot capture these effects since it neglects  $\mathcal{N}$ . Figure 18(c,d) shows the resulting (relative) error with respect to the LES reference. In proximity of the start-up vortex, the maximum

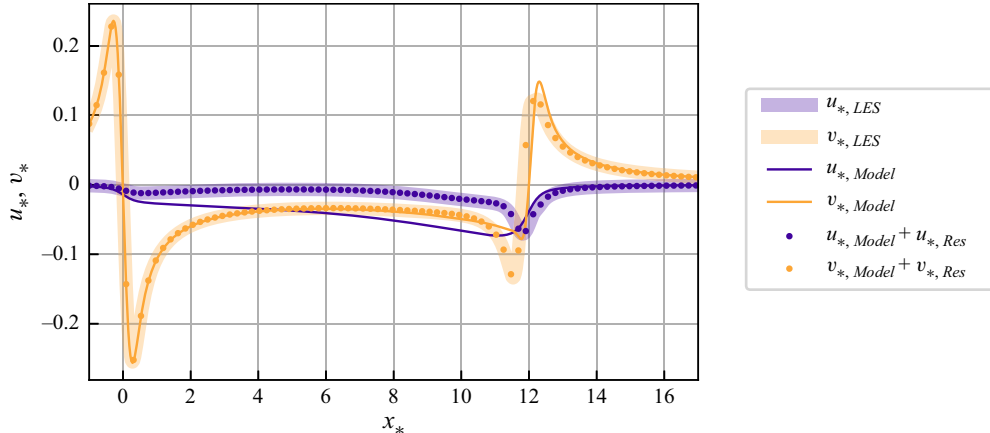


Figure 19. Comparison of the model and the LES solution for the streamwise and normal induced velocity along the curve  $(x_*, y_*) = 0^\top$  for  $\epsilon_* = 0.25$  at time instance  $t_* = 12$  (A8-Cxy-S12 case). The markers show the sum of the model solution and the velocity induced by the vorticity residual shown in figure 18(c). The residual contribution is obtained by numerical evaluation of the Biot–Savart integral.

relative error reaches more than 30 %, but it remains of the order of a few per cent in the remaining wake region between the bound and start-up vortex. We now show that this vorticity error accounts for the discrepancy of the streamwise induced velocity at the actuator point, which is observed in figure 11(a). To this end, we numerically evaluate the Biot–Savart law of the vorticity residual  $\omega_{*,\text{LES}} - \omega_{*,\text{Model}}$  to obtain the velocity residuals  $u_{*,\text{Res}}$  and  $v_{*,\text{Res}}$ . Figure 19 shows the streamwise and normal induced velocity along the wake centreline both for the model and the LES. The model correctly predicts  $v_*$  near the actuator point and in the near wake, but deviations occur farther downstream near the start-up vortex. The streamwise component  $u_*$  also deviates already in the proximity of the actuator point as observed previously. However, adding the numerically computed residual velocities to the model solution recovers the LES solution. This finding shows that the derived model solutions for the induced velocity ((3.3) and (3.10)) and the vorticity ((B6) and (B9)) are consistent and that neglecting the term  $\mathcal{N}$  explains the observed model error.

The same error analysis is also conducted for the A0-Cxy-P3-k03 case in figure 20, which features a continuous change of bound vorticity and, thus, also a continuous band of shed vorticity. The (relative) error shown in panels *c* and *d* of this figure is constrained to a region starting downstream of  $x_* = 6$ . This localisation shows that the previously observed absence of large errors in the near wake of the pitch step case is not simply due to the absence of vorticity (the start-up vortex was already advected further downstream), but that the linearised vorticity transport equation is capable of predicting an accurate trajectory of the shed vorticity in the near wake. This observation also manifests in the induced velocity distributions along the centreline shown in figure 21. The model captures the normal induced velocity accurately up to  $x_* = 6$ . The deviations farther downstream and in general for the streamwise induced velocity are again shown to be accounted for by the contribution of the vorticity residual between LES and the model.

## 7. Numerical and experimental model validation

In the two preceding sections we verified the developed model with the corresponding nonlinear ALM-LES results and quantified the error due to using the linearised governing equations for the model derivation. However, there are additional physical effects that

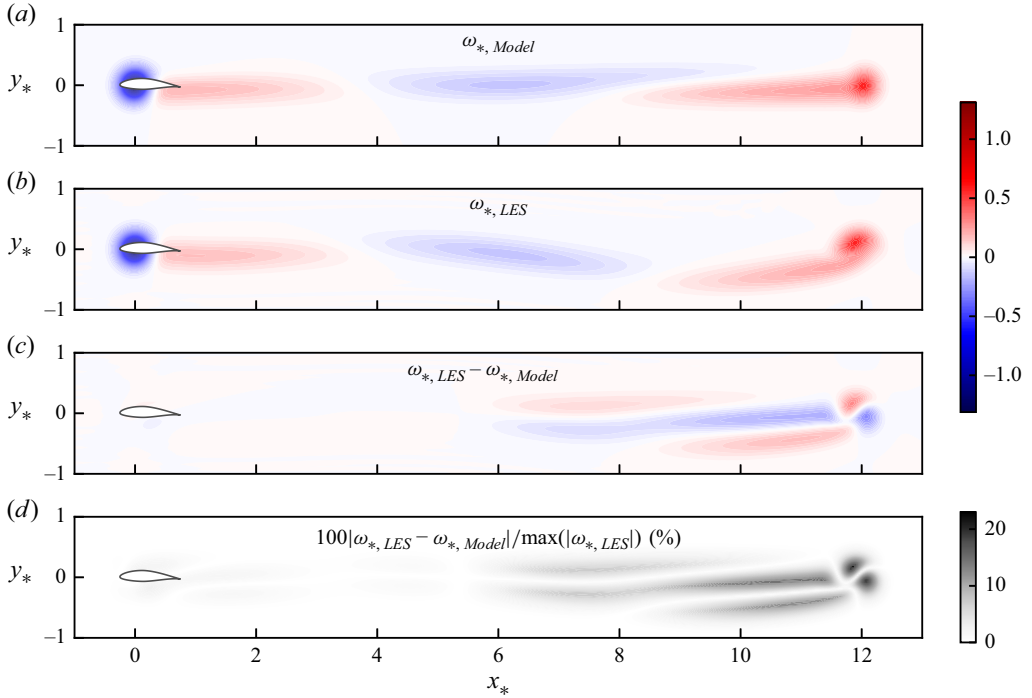


Figure 20. Model (a) and LES (b) solution for the total vorticity field of the A0-Cxy-P3-k03 case for  $\epsilon_* = 0.25$  at time instance  $t_* = 12$ . The difference between the model and LES solution is shown in (c). The relative error is shown in (d) where the reference for the normalisation of the error is the maximum value of the absolute vorticity in the  $x_* - y_*$  plane. The aerofoil modelled by the Gaussian body force is shown with a black outline. The aerofoil's quarter-chord point is located at the actuator point  $(x_*^{\text{Act}}, y_*^{\text{Act}})^\top = (0, 0)^\top$ .

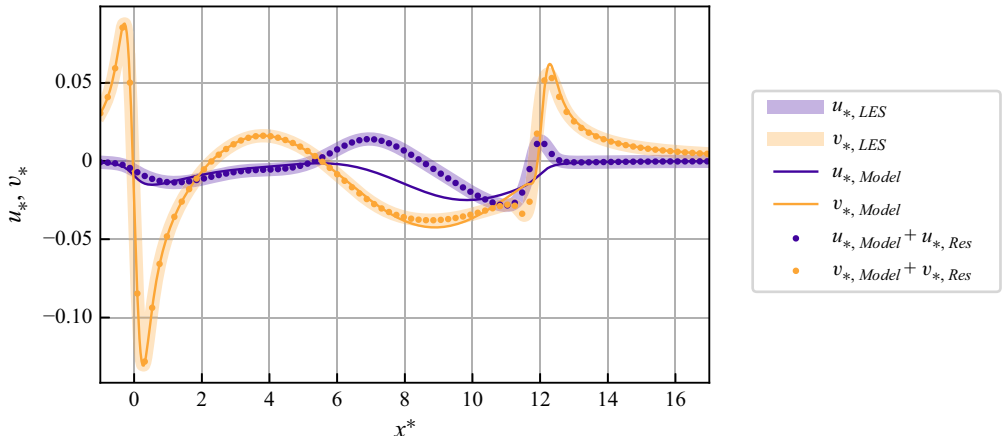


Figure 21. Comparison of the model and the LES solution for the streamwise and normal induced velocity along the curve  $(x_*, y_*) = (0, 0)^\top$  for  $\epsilon_* = 0.25$  at time instance  $t_* = 12$  (A0-Cxy-P3-k03 case). The markers show the sum of the model solution and the velocity induced by the vorticity residual shown in figure 20(c). The residual contribution is obtained by numerical evaluation of the Biot–Savart integral.

Study	Aerofoil	$Re$	$\beta^0$	$\Delta\beta$	$k$
Numerical: Motta <i>et al.</i> (2015)	NACA 00{04/12/18/24}	$\infty$	0°	1°	0.01 – 0.75
Experiment: Ōtomo <i>et al.</i> (2020)	NACA 0018	$3.2 \times 10^4$	0°	{4, 8}°	{0.22, 0.44, 0.66}

Table 2. Overview of the numerical and experimental data sets employed for the model validation. The type of aerofoil is shown together with the studied chord-based Reynolds numbers  $Re$ , operating points  $\beta^0$ , pitch amplitudes  $\Delta\beta$  and the reduced frequencies  $k$ .

are inherently not captured by the ALM and, thus, are also ignored by the derived model, which is intended to reproduce the ALM predictions. The comparison with Theodorsen theory in § 4.3 showed that the classical ALM neglects the non-circulatory contributions to the unsteady lift and also does not take into account the circulatory contribution from the pitch rate. Furthermore, Theodorsen theory itself assumes inviscid flow, approximates the aerofoil with a simple representation in terms of point vortices, neglects the aerofoil thickness and assumes the trajectory of the shed vorticity in the wake to be solely determined by the free-stream velocity (linearisation). In order to probe the impact of these model assumptions, we validate the developed model for the ALM with numerical and experimental reference data, which (partially) do not rely on the above assumptions (table 2). Doing so allows us to find answers to the two questions raised earlier, namely, is the steady-state optimal kernel width still applicable for the unsteady case, and furthermore, when does the ALM fail to predict the unsteady loading even when using the optimal kernel width?

### 7.1. Validation with inviscid (Euler) CFD

We first compare the model with numerical reference data from Motta, Guardone & Quaranta (2015). They employ a finite-volume Euler solver for moving, overset, multi-block grids to compute the loads on symmetric aerofoils in response to sinusoidal pitching motion around the quarter-chord point ( $a = -0.5$ ). The pitching motion is characterised by an operating point of  $\beta^0 = 0^\circ$ , a pitch amplitude of  $\Delta\beta = 1^\circ$  and considers the range of reduced frequencies  $k \in [0.01, 0.75]$ . The flow is approximately incompressible with a Mach number of  $Ma = 0.117$ . Four different NACA aerofoils (0004, 0012, 0018, 0024) were simulated to study the impact of aerofoil thickness on the unsteady loads and the results were compared with Theodorsen theory.

We compare in figure 22 the ALM transfer function,  $G(k)$ , for the unsteady lift with the results from Motta *et al.* (2015) obtained for their thinnest studied aerofoil (NACA 0004). In addition, the Theodorsen transfer function,  $T(k)$ , is shown. It should be noted that Motta *et al.* (2015) chose to present their results in terms of the unsteady lift coefficient normalised with the pitch amplitude ( $\Delta C_L^{us}(k)/\Delta\beta$ ) and, thus, the transfer function  $G(k)$  and  $T(k)$  need to be multiplied with the aerofoil lift slope ( $dC_L/d\alpha = 2\pi$  for the flat plate) in order to obtain the appropriate scaling. Furthermore, it should be noted that the transfer function  $G(k)$  for the ALM is also computed based on the flat plate lift slope to be consistent with Theodorsen theory. The reference data for the NACA 0004 aerofoil closely match the magnitude and phase of  $T(k)$ . Because of the good match between the thin-aerofoil CFD results and  $T(k)$ , the conclusions reached in § 4.3 regarding the limits of the ALM's applicability to model unsteady aerodynamics apply to the validation with the CFD data. A Gaussian kernel width of  $\epsilon_* \approx 0.4$  closely matches the magnitude of the unsteady lift up to  $k < 0.2$ , whereas deviations in phase occur as soon as  $k > 0$ .

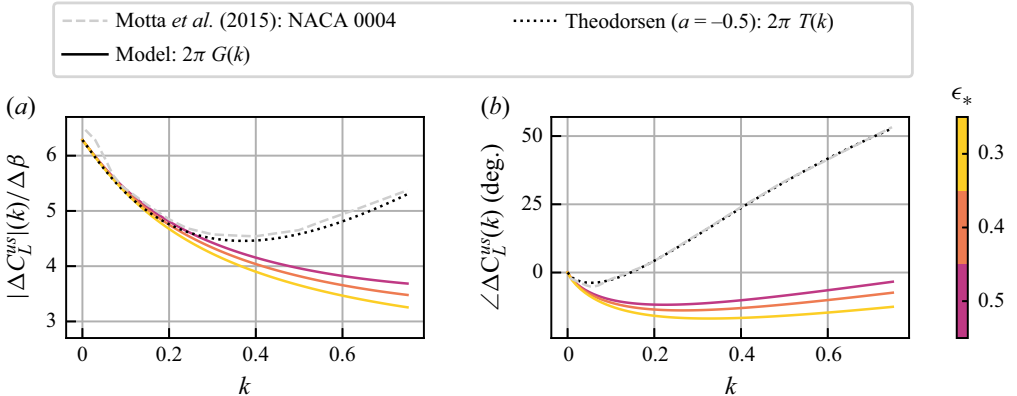


Figure 22. Magnitude (a) and phase (b) of the unsteady lift coefficient normalised with the actuation pitch amplitude  $\Delta\beta$  as function of reduced frequency  $k$ . The predictions of the model frequency domain solution assuming the lift slope of a flat plate are compared with the unsteady lift predicted by Theodorsen theory and inviscid CFD results from Motta *et al.* (2015) for a NACA 0004 aerofoil.

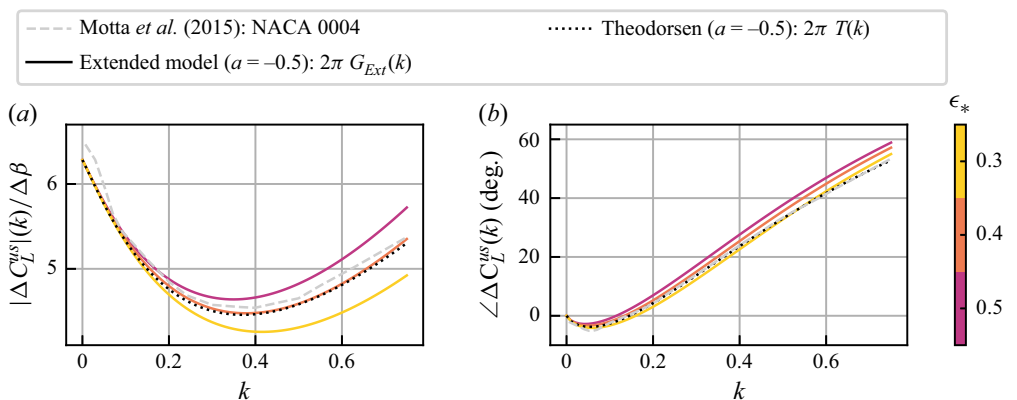


Figure 23. Magnitude (a) and phase (b) of the unsteady lift coefficient normalised with the actuation pitch amplitude  $\Delta\beta$  as function of reduced frequency  $k$ . The predictions of the extended model frequency domain solution assuming the lift slope of a flat plate are compared with the unsteady lift predicted by Theodorsen theory and inviscid CFD results from Motta *et al.* (2015) for a NACA 0004 aerofoil.

In § 4.3 we also showed that the three remaining terms modelled by Theodorsen theory, but neglected by the ALM, can be incorporated into an extended ALM transfer function  $G_{Ext}(k)$  (4.15). In figure 23, the previous comparison with the reference data from Motta *et al.* (2015) for the NACA 0004 aerofoil is repeated for  $G_{Ext}(k)$ . It can be seen that  $G_{Ext}(k; \epsilon_* = 0.4)$  closely reproduces the prediction from Theodorsen theory and, thus, also leads to an accurate magnitude and phase prediction compared with the CFD reference. While the objective of the present study is to reproduce the behaviour of the classical ALM with a simple model, this result highlights avenues for future work to incorporate the non-circulatory terms,  $T_{NC}^{\dot{\beta}}$  and  $T_{NC}^{\ddot{\beta}}$ , and the pitch rate dependent circulatory term,  $T_C^{\dot{\beta}}$ , into the ALM formulation in order to increase the bounds of the ALM's applicability to unsteady aerodynamics beyond  $k = 0.2$ .

The presented comparison with inviscid CFD and Theodorsen theory leads to recommendations regarding the optimal kernel width in order to accurately capture

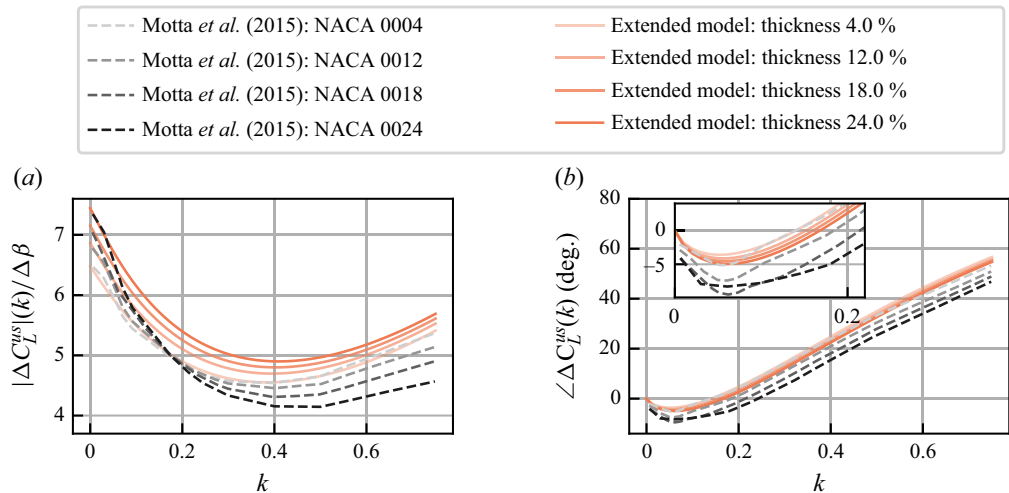


Figure 24. Magnitude (a) and phase (b) of the unsteady lift coefficient normalised with the actuation pitch amplitude  $\Delta\beta$  as function of reduced frequency  $k$ . The predictions of the extended model frequency domain solution are shown for  $\epsilon_* = 0.4$ . The employed lift slope varies with the aerofoil thickness according to  $dC_L/d\alpha = 2\pi(1 + 0.77d/c)$ . Results are compared with inviscid CFD results from Motta *et al.* (2015) for the NACA 0004, NACA 0012, NACA 0018 and NACA 0024 aerofoils.

unsteady aerodynamic effects with the classical ALM based on point velocity sampling. We find that the reference data are closely matched up to  $k < 0.2$  for a kernel width in the range  $\epsilon_* \in [0.3, 0.5]$ . Based on the validation of the extended ALM transfer function  $G_{Ext}(k)$ , a kernel width of  $\epsilon_* \approx 0.4$  provides a good match with Theodorsen theory and CFD throughout the frequency range  $k \in [0, 0.75]$ . These identified values for the optimal unsteady kernel width are slightly higher than the range of the optimal kernel width found for steady conditions  $\epsilon_{*,Opt} \in [1/8, 1/4]$  (Shives & Crawford 2013; Martínez-Tossas *et al.* 2017). However, we note that when using a Gaussian kernel with different widths in the chord and thickness directions, Martínez-Tossas *et al.* (2017) found that the optimal width along the chord direction is approximately  $\epsilon_* \approx 0.3$  for thin aerofoils. Since the chord is the principal direction in the unsteady problem, it is reasonable for the optimal width to scale accordingly. Given that practical ALM-LES for wind turbine/farm modelling typically operate with kernel widths that are an order of magnitude larger, the difference between the identified optimal kernel width for steady and unsteady aerodynamics is rather small. Nevertheless, future work should explore if this difference persists when considering an advanced ALM formulation based on integral velocity sampling as proposed by Churchfield *et al.* (2017).

Lastly, Motta *et al.* (2015) also studied the unsteady loads on NACA 0012, 0018 and 0024 aerofoils and showed that the increasing non-dimensional aerofoil thickness of up to  $d/c = 24\%$  challenges the flat plate assumption made by Theodorsen theory. Figure 24 shows that this equally applies to the ALM. Figure 24(a) shows that the steady lift magnitude,  $|\Delta C_L^{us}|(k = 0)$ , continuously increases with the aerofoil thickness. In fact the term  $\Delta C_L^{us}(k = 0)/\Delta\beta$  is the lift slope of the aerofoil, which can be approximated with the relation  $dC_L/d\alpha = 2\pi(1 + 0.77d/c)$  (Motta *et al.* 2015). The only way the aerofoil thickness enters the ALM is via the lift(-slope) input. Thus, we use the relation between thickness and lift slope given above to determine varying lift slope inputs for  $G_{Ext}(k)$  in order to model the impact of increasing aerofoil thickness. Comparing the unsteady lift magnitude in figure 24(a) shows that the  $G_{Ext}(k)$  now more closely matches the CFD

results in proximity of  $k = 0$  than when using the flat plate lift slope to ensure consistency with Theodorsen theory (compare with figure 23). However, these deviations are small compared with the deviations between the CFD and ALM results for larger aerofoil thicknesses of 12 %–24 %. The increased damping of the lift magnitude predicted by CFD is not captured by the ALM, in particular, as soon as  $k > 0.05$ . Similar conclusions are found for the phase in figure 24(b). The CFD results predict a shift of the phase inversion point to larger  $k$  as the thickness increases. This trend is only qualitatively captured by the ALM, but both the maximum phase lag and the reduced frequency corresponding to the phase inversion point are quantitatively underestimated.

## 7.2. Validation with experiment at $Re = 32\,000$

Lastly, we validate the ALM predictions with the experimental data set from Ōtomo *et al.* (2020). They studied a NACA 0018 aerofoil with periodic smoothed triangular pitching kinematics at  $Re = 32\,000$ . Hence, this validation data set also probes the model assumption of inviscid flow, and furthermore, the model is tested for actuation signals that are more complex than mono-frequency sinusoids. The triangular pitching kinematics are characterised by an operating point of  $\beta^0 = 0^\circ$ , pitch amplitudes of  $\Delta\beta \in \{4^\circ, 8^\circ\}$  and periods corresponding to the reduced frequencies  $k \in \{0.22, 0.44, 0.66\}$ . The location of the pitching axis is the quarter-chord point ( $a = -0.5$ ). Ōtomo *et al.* (2020) compared their experimental results also to predictions from Theodorsen theory by considering the superposition of the individual Theodorsen solutions corresponding to the twenty leading Fourier harmonics.

The temporal evolution of the unsteady lift coefficient in response to the smoothed triangular pitching kinematics is shown for one period  $T_{p*}$  in figure 25 and the corresponding maxima of the lift coefficient are summarised in figure 26. The experimental data and the Theodorsen solution are compared with the time-domain solution of the developed model. The model solution is computed for the kernel width  $\epsilon_* = 0.4$ , which was determined as the recommended kernel width for unsteady conditions in the previous validation section. We start by focusing on the case  $k = 0.22/\Delta\beta = 4^\circ$  (figure 25a), which can be seen as the limit case for the ALM's applicability to unsteady aerodynamics given the preceding comparison with Theodorsen theory and the CFD results from Motta *et al.* (2015) in § 7.1. The Theodorsen solution is also shown split into the non-circulatory and circulatory contributions to visualise their relative importance. The non-circulatory term proportional to the pitch acceleration is zero within the linear parts of the pitch actuation signal due to the constant pitch rate and, thus, only contributes close to the extreme values of the pitch. It can be seen that the ALM predicts a slightly smaller unsteady lift magnitude than Theodorsen theory, which can be attributed to the observation that the non-circulatory terms neglected by the ALM reduce the damping of the unsteady lift (also recall figure 4). Due to the inclusion of the non-circulatory terms, the Theodorsen theory predicts a positive phase shift with respect to the pitch actuation signal with the fundamental frequency of  $k = 0.22$ , whereas the ALM still predicts a small phase lag. The experimental data shows the overall largest damping and phase lag. Motta *et al.* (2015) also studied the effect of including viscosity in their CFD study such that  $Re = 10^6$  for a NACA 0018 aerofoil. They observed a reduced maximum lift coefficient for the viscous results compared with the inviscid reference. Furthermore, experiments conducted by Mackowski & Williamson (2015) for a NACA 0012 aerofoil subject to sinusoidal pitching at  $Re = 16\,600$  also showed stronger damping, i.e. smaller peak lift coefficient values, compared with Theodorsen theory for the pitch amplitudes  $\Delta\beta \in \{2, 4, 8\}^\circ$  in the range  $k \in [0, 1]$ . The increased deviation between the inviscid ALM

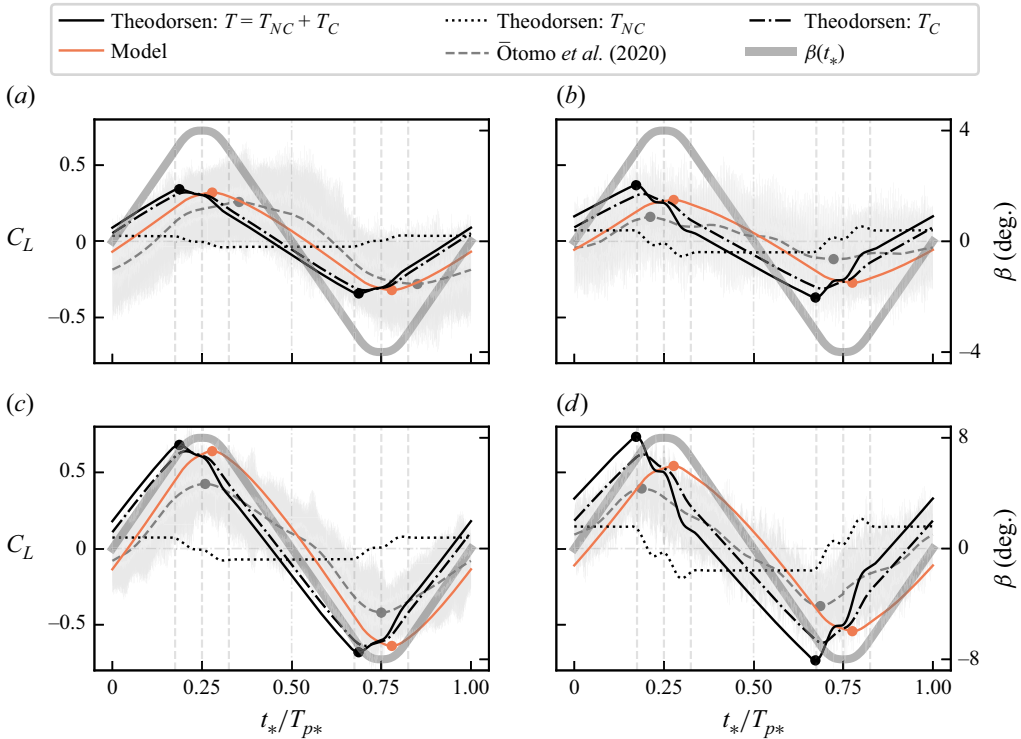


Figure 25. One period of the unsteady lift coefficient in response to smoothed triangular pitching kinematics with  $k = 0.22$  (a,c) and  $k = 0.44$  (b,d) with actuation amplitudes of  $\Delta\beta = 4^\circ$  and  $\Delta\beta = 8^\circ$ . The predictions of the model time domain solution are shown for  $\epsilon_* = 0.4$  using the lift coefficient of a flat plate. For reference, the experimental results from Otomo *et al.* (2020) are shown (the shaded grey area denotes the 95 % confidence interval). In addition, the predictions of Theodorsen theory are shown, where the non-circulatory and circulatory contributions are also shown separately. The thick semi-transparent line indicates the time series of the pitch actuation signal. Dots mark the maxima and minima of the signals.

and Theodorsen solutions compared with the experimental data from Otomo *et al.* (2020) thus is in agreement with the observations made in the two aforementioned studies. It should be further pointed out that one should not conclude from the comparison with the experiment that the ALM prediction is more accurate than Theodorsen theory. The closer match between the ALM and the experiment is rather likely due to fortunate cancellation of the modelling errors due to neglecting viscosity, but in addition also the three terms  $T_{NC}^\beta$ ,  $T_{NC}^\beta$  and  $T_C^\beta$  that in turn are captured by Theodorsen theory.

Doubling the pitch amplitude (the case  $k = 0.22/\Delta\beta = 8^\circ$  shown in figure 25c) leads to doubled lift magnitudes predicted by ALM and Theodorsen theory, which is consistent with their linear nature. In contrast, the increase in lift magnitude seen in the experiment is only 60 %. Furthermore, phase predictions of the linear models are unaltered, whereas the experiment shows a gain in phase such that the unsteady lift is almost in phase with the pitch actuation. Further increasing the fundamental frequency of the pitch actuation to  $k = 0.44$  increases the importance of the non-circulatory terms, where the unsteady lift signals from Theodorsen theory and experiment now are ahead of the pitch actuation (figure 25b,d).

As a summary of the observations made above, the maximum lift coefficients for the ALM, Theodorsen theory and the experiment are shown as a function of the reduced

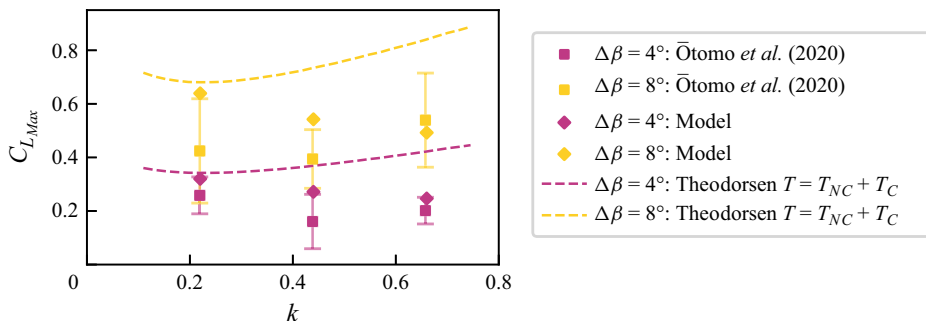


Figure 26. Maximum unsteady lift coefficient resulting from the smoothed triangular pitching kinematics with amplitude  $\Delta\beta = 4^\circ$  and  $\Delta\beta = 8^\circ$ . The predictions of the model time domain solution are shown for  $\epsilon_* = 0.4$  using the lift coefficient of a flat plate. For reference, the experimental results of Ōtomo *et al.* (2020) are shown (error bars denote the 95 % confidence interval). In addition, the predictions of Theodorsen theory are shown.

frequency  $k$  in figure 26. It can be concluded that for the case of  $k = 0.22/\Delta\beta = 4^\circ$  both the ALM and Theodorsen theory still provide reasonable lift predictions despite the low Reynolds number  $Re = 32\,000$  of the experiment. In this light, the observed errors can be seen as an upper bound, given that for wind energy purposes, where the ALM finds its most use, chord-based Reynolds numbers are two orders of magnitude larger. It should be again stressed that the apparent better match between the ALM and experiment compared with Theodorsen theory is expected to stem from the lack of modelling the terms  $T_{NC}^{\dot{\beta}}$ ,  $T_{NC}^{\ddot{\beta}}$  and  $T_C^{\dot{\beta}}$ . Thus, the experimental validation affirms the conclusions drawn from the ALM-Theodorsen comparison (§ 4.3) and from the validation with inviscid CFD results (§ 7.1), namely that the ALM can capture unsteady aerodynamic effects up to  $k \approx 0.2$  given that the Gaussian kernel width is close to the determined optimum  $\epsilon_* \approx 0.4$ ; the aerofoil thickness is limited; and errors in phase of approximately twenty degrees can be accepted.

## 8. Conclusions

In this study we assessed the ability of the ALM to capture the unsteady aerodynamic effects of induced velocity due to shed vorticity. We focused on the simplified two-dimensional problem of an aerofoil represented by an unsteady Gaussian body force. The objective was to determine the unsteady loading on the aerofoil in response to generic unsteady pitch actuation with an explicit dependence on the Gaussian kernel width. This problem formulation thereby links the ALM to the theories developed by Wagner (1925) and Theodorsen (1935) for the unsteady inviscid thin-aerofoil problem. A linearised vorticity transport equation was obtained from the Euler equations subject to an unsteady Gaussian body force, which enabled the derivation of theoretical solutions for the induced velocity along the wake centreline and the complete two-dimensional vorticity field. The former solution takes the form of a Duhamel's integral involving an indicial response function. Based on the theoretical velocity solutions, a model for the unsteady aerofoil loading was derived. Its solution was obtained in the time domain by solving a root-finding problem for the flow angle as well as in the frequency domain by deriving the system's closed-loop transfer function mapping from the quasi-steady to the unsteady lift force. The closed-loop transfer function is parameterised by the Gaussian kernel width and, thus, explicitly shows its impact on the amplitude modulation and phase lag of the unsteady lift as a function of the reduced frequency.

The model was verified with nonlinear reference data obtained by means of ALM-LES. The verification study considered both pitch step and periodic pitch actuation cases, where the model was tested within the linear region of the aerofoil's lift curve. The relative errors for the angle of attack were on the order of tenths of a per cent. The model was shown to accurately capture the time evolution of the induced normal velocity, the angle of attack and the streamwise and normal force coefficients within the considered range of kernel widths  $\epsilon_* \in [0.25, 4.0]$  and reduced frequencies  $k \in \{0.1, 0.2, 0.3, 0.6\}$ . However, a mismatch between ALM-LES and the model was observed for the streamwise induced velocity in the case of combined streamwise and normal forcing. This mismatch was shown to be a direct consequence of the linearisation of the vorticity transport equation during the model derivation by computing the induced velocity corresponding to the vorticity residual between the nonlinear ALM-LES results and the theoretical vorticity solution.

The derived model was then used to validate the ALM's ability to model unsteady aerodynamics in attached flow conditions below stall. The comparison with Theodorsen theory showed that the ALM does not capture the contributions of the non-circulatory terms and the circulatory contribution of the pitch rate. This conclusion was confirmed by further validation with reference to results obtained by means of inviscid CFD using body fitted grids. Two main conclusions were drawn from this validation. Firstly, the optimal kernel width for modelling unsteady aerodynamics with the classical ALM based on point velocity sampling is  $\epsilon_* \approx 0.4$ . This value is still on the order  $\epsilon_* = \mathcal{O}(10^{-1})$ , but slightly larger than the range  $\epsilon_* \in [1/8, 1/4]$  previously identified for the optimal steady-state isotropic Gaussian kernel width. Secondly, the ALM can accurately predict the magnitude of the unsteady loading up to reduced frequencies of  $k \approx 0.2$  when employing a kernel width of the order of the identified optimum for unsteady aerodynamics. However, small errors in phase occur as soon as  $k > 0$ , where the error is about twenty degrees at  $k = 0.2$ . Finally, validation with experimental data for an aerofoil executing smoothed triangular pitching kinematics at  $Re = 32\,000$  further pointed towards the previously identified threshold frequency of  $k \approx 0.2$  beyond which the ALM is not sufficient to capture unsteady effects.

Based on the results, we have identified three key directions for future work. Firstly, the model derivation is currently based on a linearisation point equivalent to undisturbed (vorticity-free) flow. Incorporating a flexible linearisation point by using the corresponding steady-state solution could improve the model's capabilities of predicting the trajectory of the shed vorticity in the wake. A second path is to extend the model to three dimensions, e.g. to obtain an unsteady three-dimensional filtered lifting line solution, extending the steady-state solution derived by Martínez-Tossas & Meneveau (2019). Finally, this unsteady three-dimensional filtered lifting line solution could then be employed as a correction for coarse grid ALM-LES.

**Acknowledgements.** E.T. would like to thank the Wind Energy Science group at the National Renewable Energy Laboratory (NREL) for enabling his research stay at NREL in Boulder, during which most progress on this work was made and for their warm hospitality. E.T.'s fellow PhD colleagues David Fidalgo Domingos, Marcus Becker and Daniel van den Berg are thanked for their ideas that ultimately lead to the development of the frequency domain solution of the model. The authors would further like to acknowledge the very helpful discussions with Nathaniel Wei and Shūji Otomo.

**Funding.** This work is part of the Hollandse Kust Noord wind farm innovation program where CrossWind C.V., Shell, Eneco and Siemens Gamesa are teaming up; funding for the PhDs and PostDocs was provided by CrossWind C.V. and Siemens Gamesa. We further would like to acknowledge SURF for the computational resources made available on the Dutch national supercomputer Snellius (grant number: EINF-6784). This work was authored in part by the National Renewable Energy Laboratory, operated by Alliance for Sustainable

Energy, LLC, for the U.S. Department of Energy (DOE) under Contract No. DE-AC36-08GO28308. Funding provided by the U.S. Department of Energy Office of Energy Efficiency and Renewable Energy Wind Energy Technologies Office. The views expressed in the article do not necessarily represent the views of the DOE or the U.S. Government. The U.S. Government retains and the publisher, by accepting the article for publication, acknowledges that the U.S. Government retains a non-exclusive, paid-up, irrevocable, worldwide license to publish or reproduce the published form of this work, or allow others to do so, for U.S. Government purposes.

**Declaration of interests.** The authors report no conflict of interest.

**Author contributions.** E.T, G.D., J.W.W. and L.M. derived the model solutions. E.T. and L.M. implemented the model solutions and post-processing code. M.K. and E.T. made the necessary changes to AMR-Wind to enable the LES reference simulations. E.T. set up and performed the LES simulations with the help of L.M. and M.K.. E.T. conducted the model validation. All authors contributed to analysing data, reaching conclusions and writing the paper.

## Appendix A. Solving the linearised vorticity transport equation

In order to solve (2.3), one can exploit its advection character by considering solutions along spatio-temporal curves given by  $X(s) = x_* + s$  and  $T(s) = t_* + s$  (neglecting the  $y_*$  dependence, which is not relevant for the derivation). Differentiation of the solution along these curves yields

$$\frac{d}{ds}\omega_*(X(s), T(s)) = \frac{\partial\omega_*}{\partial x} \frac{dX}{ds} + \frac{\partial\omega_*}{\partial t} \frac{dT}{ds} = \frac{\partial\omega_*}{\partial x} + \frac{\partial\omega_*}{\partial t} = F(X(s), T(s)), \quad (\text{A1})$$

where  $F(X(s), T(s))$  represents the right-hand side of (2.3). Subsequent integration from  $T(s = -t_*) = 0$  to  $T(s = 0) = t_*$  provides

$$\int_{-t_*}^0 \frac{d}{ds}\omega_*(X(s), T(s)) ds = \omega_*(x_*, t_*) - \omega_*(x_* - t_*, 0) = \int_{-t_*}^0 F(x_* + s, t_* + s) ds. \quad (\text{A2})$$

Using the transformation  $s' = t_* + s$  ( $ds' = ds$ ) and subsequently denoting  $s'$  again as  $s$ , the solution with the explicit  $y_*$  dependence is obtained as shown in (2.5).

## Appendix B. The vorticity field created by an unsteady Gaussian body force

The derivations in § 3 bypass the need to calculate an explicit vorticity solution and, thus, avoid the need for expressing the forcing in terms of a given set of basis functions. This approach allows the computation of the unsteady loading on an aerofoil subject to a generic pitch actuation, as shown in § 4. However, it is instructive to study not only the influence of the Gaussian kernel width on the unsteady loading but also the unsteady vorticity field forming around the aerofoil for the following two reasons. First, the vorticity field offers an explanation for the magnitude and phase modulation introduced to the unsteady loading for a given Gaussian kernel width and reduced frequency. Second, the vorticity solution can be utilised to assess the spatial and temporal nature of the modelling error caused by linearising the vorticity transport equation (2.2) by computing the nonlinear vorticity residual with respect to the reference LES data.

Thus, in the following an unsteady vorticity solution for (2.3) is derived, which requires expressing the forcing time histories  $C_x(t_*)$  and  $C_y(t_*)$  as a Fourier series. Then, the solution from § 4.1 can be utilised as a starting point to obtain the forcing time histories for a given pitch actuation signal defined on  $t_* \in [0, T_*]$ , incorporating the feedback effect of the shed vorticity. Subsequently, the forcing time histories are expressed as discrete Fourier series

$$C_x(t_*) = C_x^0 + \sum_{n=1}^N (\alpha_x^n \cos(2\pi n t_*/T_*) + \beta_x^n \sin(2\pi n t_*/T_*)), \quad (\text{B1})$$

$$C_y(t_*) = C_y^0 + \sum_{n=1}^N (\alpha_y^n \cos(2\pi n t_*/T_*) + \beta_y^n \sin(2\pi n t_*/T_*)), \quad (\text{B2})$$

where  $\alpha_x^n$ ,  $\beta_x^n$ ,  $\alpha_y^n$  and  $\beta_y^n$  are the real Fourier coefficients for the streamwise and normal forcing, respectively. By exploiting the linearity of (2.3), one may consider the solution for each Fourier basis function separately and obtain the complete solution by superposition. To this end, consider the combined streamwise and normal forcing term (right-hand side of (2.3)) for a single frequency component to be

$$\begin{aligned} F^n(x_*, y_*, t_*) = & \frac{-y_*(\alpha_x^n \cos(\sigma_*^n t_*) + \beta_x^n \sin(\sigma_*^n t_*))}{\pi \epsilon_*^4} e^{-(x_*^2 + y_*^2)/\epsilon_*^2} \\ & + \frac{x_*(\alpha_y^n \cos(\sigma_*^n t_*) + \beta_y^n \sin(\sigma_*^n t_*))}{\pi \epsilon_*^4} e^{-(x_*^2 + y_*^2)/\epsilon_*^2}, \end{aligned} \quad (\text{B3})$$

where  $\sigma_*^n = 2\pi n t_*/T_*$  is the harmonic angular frequency.

The complete vorticity solution is then obtained by superposing three contributions: the unsteady vorticity contributions from each non-zero frequency  $\omega_*^n$ , the contributions  $\omega_*^0$  from the zero frequency components  $C_x^0$  and  $C_y^0$ , and, if applicable, the contribution from the initial vorticity field  $\omega_*^{IC}$ , which in this work is considered to be the vorticity field corresponding to the steady-state solution ((8) and (15) from Martínez-Tossas *et al.* 2017). In the following, we derive the missing solutions for the first two contributions for normal and streamwise forcing and assemble the complete solutions.

### B.1. Vorticity due to normal forcing

The vorticity solution accounting for the unsteady non-zero frequency contributions ( $n > 0$ ) of the normal forcing is obtained by inserting the normal forcing component of (B3) into the integral in (2.5) to obtain

$$\omega_*^n = \int_{x_* - t_*}^{x_*} \xi \frac{\alpha_y^n \cos[\sigma_*^n(\xi - x_* + t_*)] + \beta_y^n \sin[\sigma_*^n(\xi - x_* + t_*)]}{\pi \epsilon_*^4} e^{-(\xi^2 + y_*^2)/\epsilon_*^2} d\xi, \quad (\text{B4})$$

where the transformation  $\xi = x_* + (s - t_*)$  ( $d\xi = ds$ ) is used. For the resulting integral, an analytical solution can be found. The solution corresponding to the zero frequency component of the unsteady forcing ( $n = 0$ ) is obtained by inserting the forcing  $C_y^0$  instead of the trigonometric functions into the integral in (2.5), which then can readily be solved to obtain

$$\omega_*^0 = -\frac{C_y^0}{2\pi \epsilon_*^2} e^{-(x_*^2 + y_*^2)/\epsilon_*^2} + \frac{C_y^0}{2\pi \epsilon_*^2} e^{-[(x_* - t_*)^2 + y_*^2]/\epsilon_*^2}. \quad (\text{B5})$$

Finally, all three vorticity contributions can be combined to end up with the vorticity solution given an unsteady normal forcing  $C_y(t_*)$  and subject to the assumption that  $C_y(t_*)$  can be expressed as a discrete Fourier series:

$$\begin{aligned}
 \omega(x_*, y_*, t_*) &= \omega_*^{IC} + \omega_*^0 + \omega_*^n \\
 &= -\frac{C_y^{IC}}{2\pi\epsilon_*^2} e^{-[(x_* - t_*)^2 + y_*^2]/\epsilon_*^2} \\
 &\quad - \frac{C_y^0}{2\pi\epsilon_*^2} e^{-(x_*^2 + y_*^2)/\epsilon_*^2} + \frac{C_y^0}{2\pi\epsilon_*^2} e^{-[(x_* - t_*)^2 + y_*^2]/\epsilon_*^2} \\
 &\quad + \sum_{n=1}^N \left\{ -\frac{\alpha_y^n \cos(\sigma_*^n t_*) + \beta_y^n \sin(\sigma_*^n t_*)}{2\pi\epsilon_*^2} e^{-(x_*^2 + y_*^2)/\epsilon_*^2} \right. \\
 &\quad \left. + \frac{\alpha_y^n}{2\pi\epsilon_*^2} e^{-[(x_* - t_*)^2 + y_*^2]/\epsilon_*^2} \right. \\
 &\quad \left. + \frac{\sigma_*^n}{4\pi\epsilon_*^2} e^{-y_*^2/\epsilon_*^2} \left\{ (\alpha_y^n i + \beta_y^n) e^{i\sigma_*^n(-x_* + t_*)} \left( -\frac{1}{2} i \sqrt{\pi} \epsilon_* e^{-1/4(\sigma_*^n)^2 \epsilon_*^2} \right) \times \right. \right. \\
 &\quad \left. \left[ \operatorname{erfi}\left(\frac{\sigma_*^n \epsilon_*}{2} + \frac{i x_*}{\epsilon_*}\right) - \operatorname{erfi}\left(\frac{\sigma_*^n \epsilon_*}{2} + \frac{i(x_* - t_*)}{\epsilon_*}\right) \right] \right. \\
 &\quad \left. + (-\alpha_y^n i + \beta_y^n) e^{-i\sigma_*^n(-x_* + t_*)} \left( \frac{1}{2} i \sqrt{\pi} \epsilon_* e^{-1/4(\sigma_*^n)^2 \epsilon_*^2} \right) \times \right. \\
 &\quad \left. \left[ \operatorname{erfi}\left(\frac{\sigma_*^n \epsilon_*}{2} - \frac{i x_*}{\epsilon_*}\right) - \operatorname{erfi}\left(\frac{\sigma_*^n \epsilon_*}{2} - \frac{i(x_* - t_*)}{\epsilon_*}\right) \right] \right\}. \quad (B6)
 \end{aligned}$$

It can be noted that in the case of a constant forcing and an already established bound vortex (i.e.  $C_y^{IC} = C_y^0$ ) the solution simply reduces to the steady-state solution derived in Martínez-Tossas *et al.* (2017).

## B.2. Vorticity due to streamwise forcing

The vorticity solution accounting for the unsteady non-zero frequency contributions ( $n > 0$ ) of the streamwise forcing is obtained by inserting the streamwise forcing component of (B3) into the integral in (2.5). Making use again of the transformation  $\xi = x_* + (s - t_*)$ , the integral reads as

$$\omega_*^n = -\frac{y_*}{\pi\epsilon_*^4} \int_{x_* - t_*}^{x_*} (\alpha_x^n \cos[\sigma_*^n(\xi - x_* + t_*)] + \beta_x^n \sin[\sigma_*^n(\xi - x_* + t_*)]) e^{-(\xi^2 + y_*^2)/\epsilon_*^2} d\xi, \quad (B7)$$

for which an analytical solution can be found. The solution corresponding to the zero frequency component ( $n = 0$ ) of the unsteady forcing is obtained by inserting the forcing  $C_x^0$  instead of the trigonometric functions into the integral in (2.5), which can then be solved to obtain

$$\omega_*^0 = \frac{C_x^0}{2\sqrt{\pi}\epsilon_*^3} y_* e^{-y_*^2/\epsilon_*^2} \left[ \operatorname{erf}\left(\frac{x_* - t_*}{\epsilon_*}\right) - \operatorname{erf}\left(\frac{x_*}{\epsilon_*}\right) \right]. \quad (B8)$$

Combining all three contributions leads to the complete vorticity solution resulting from periodic streamwise forcing  $C_x(t_*)$ :

$$\begin{aligned}
 \omega(x_*, y_*, t_*) &= \omega_*^{IC} + \omega_*^0 + \omega_*^n \\
 &= -\frac{C_x^{IC}}{2\sqrt{\pi}\epsilon_*^3} y_* e^{-y_*^2/\epsilon_*^2} \left[ 1 + \operatorname{erf}\left(\frac{x_* - t_*}{\epsilon_*}\right) \right]
 \end{aligned}$$

$$\begin{aligned}
 & + \frac{C_x^0}{2\sqrt{\pi}\epsilon_*^3} y_* e^{-y_*^2/\epsilon_*^2} \left[ \operatorname{erf} \left( \frac{x_* - t_*}{\epsilon_*} \right) - \operatorname{erf} \left( \frac{x_*}{\epsilon_*} \right) \right] \\
 & + \sum_{n=1}^N \left\{ -\frac{y_*}{2\pi\epsilon_*^4} e^{-y_*^2/\epsilon_*^2} \left\{ (\alpha_x^n - i\beta_x^n) e^{i\sigma_*^n(-x_*+t_*)} \left( -\frac{1}{2} i \sqrt{\pi} \epsilon_* e^{-1/4(\sigma_*^n)^2 \epsilon_*^2} \right) \times \right. \right. \\
 & \quad \left[ \operatorname{erfi} \left( \frac{\sigma_*^n \epsilon_*}{2} + \frac{i x_*}{\epsilon_*} \right) - \operatorname{erfi} \left( \frac{\sigma_*^n \epsilon_*}{2} + \frac{i(x_* - t_*)}{\epsilon_*} \right) \right] \\
 & \quad \left. \left. + (\alpha_x^n + i\beta_x^n) e^{-i\sigma_*^n(-x_*+t_*)} \left( \frac{1}{2} i \sqrt{\pi} \epsilon_* e^{-1/4(\sigma_*^n)^2 \epsilon_*^2} \right) \times \right. \right. \\
 & \quad \left. \left. \left[ \operatorname{erfi} \left( \frac{\sigma_*^n \epsilon_*}{2} - \frac{i x_*}{\epsilon_*} \right) - \operatorname{erfi} \left( \frac{\sigma_*^n \epsilon_*}{2} - \frac{i(x_* - t_*)}{\epsilon_*} \right) \right] \right\} \right\}. \quad (B9)
 \end{aligned}$$

An observation similar to the normal forcing case can be made. In the case of constant forcing and an already established vorticity (i.e.  $C_x^{IC} = C_x^0$ ), the solution simply reduces to the steady-state solution derived in Martínez-Tossas *et al.* (2017).

### Appendix C. A note on velocity sampling in the ALM

Both the time and frequency domain solutions of the developed model compute the forcing based on the flow angle determined at the actuator point. This approach was introduced in the foundational ALM work by Sørensen & Shen (2002). Nevertheless, there is a difference in the definition of the velocity magnitude used for the force calculation between the derived theoretical solutions and the common ALM implementation in LES codes. In principle, the lift and drag coefficients used in step (ii) of the algorithm outlined in § 4.1 are defined for the free-stream velocity  $U_\infty$ . Since the characteristic velocity scale to non-dimensionalise the equations in this work is chosen to be  $U_\infty$ , the derived solutions are consistent with this definition. However, common ALM implementations in LES codes not only use the local velocity  $\mathbf{u}_*^{LES}$  at the actuator point to determine the flow angle for evaluation of the force coefficients but also use its magnitude to directly compute the force, e.g. for the lift force, one would have  $F_L^{LES} \propto |\mathbf{u}_*^{LES}|^2 C_L(\alpha)$ . This velocity is affected by the induced velocities such that  $|\mathbf{u}_*^{LES}| = ((1 + u_*^{LES}(0, 0, t_*))^2 + v_*^{LES}(0, 0, t_*)^2)^{1/2}$  and, thus, in case of a non-zero drag coefficient or shed vorticity, it is  $|\mathbf{u}_*^{LES}| \neq 1$ , where it should be noted that, for small induced velocities,  $|\mathbf{u}_*^{LES}| \approx |1 + u_*^{LES}(0, 0, t_*)|$ . However, the force calculation should be based on the free-stream velocity according to  $F_L \propto C_L(\alpha)$ .

Martínez-Tossas *et al.* (2017) and Caprace *et al.* (2020) proposed corrections that are used to determine an estimate of the free-stream velocity solely based on the locally sampled velocity at the actuator point. Specifically for this work, this would mean that (3.14) for  $u_*$  at the actuator point would be employed to obtain the estimate  $U_\infty^{Est} \approx |\mathbf{u}^{LES} - u_*(0, 0, t_*)\mathbf{i}|$ . In the present work, this issue can be circumvented for the reference LES simulations carried out in § 5, since the free-stream velocity  $U_\infty$  is known and, thus, can be directly used for the force calculation. If, on the other hand, in the LES the force coefficients would be directly evaluated with the locally sampled velocity magnitude, an additional error between model and LES would be introduced as  $F_L^{LES}/F_L = |\mathbf{u}^{LES}|^2 \approx (1 + u_*^{LES}(0, 0, t_*))^2$ .

### Appendix D. Grid and domain size convergence of the LES set-up

This appendix motivates the chosen LES set-up in § 5.2 by studying the convergence of the angle of attack time history at the actuator point both with grid and domain size.

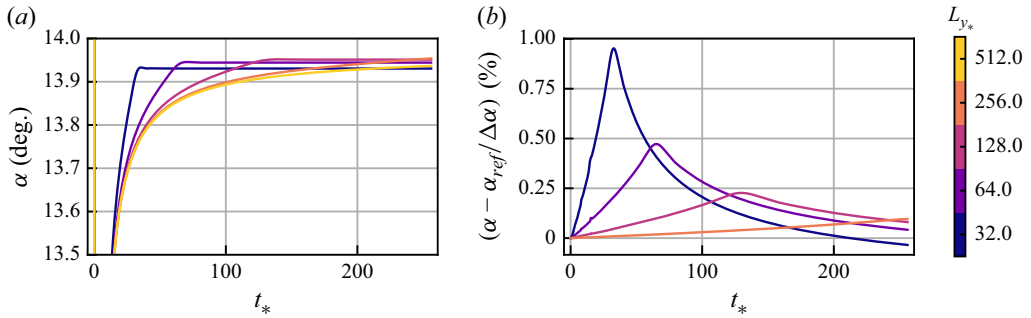


Figure 27. Domain size convergence study for case A14-Cxy-S18 using  $\epsilon_* = 0.25$ . The simulation time is  $T_* = 256$ , and the resolution of the most inner refinement is  $\epsilon_*/\Delta x_* = 4$ . (a) Angle of attack for the range of semi-domain heights  $L_{y_*} = 32$  to  $L_{y_*} = 512$ , where the upstream and downstream fetch are scaled accordingly as described in § 5.2. (b) Relative error based on the angle of attack step magnitude  $\Delta\alpha = 18^\circ$ . The reference case for the calculation of the error is  $L_{y_*} = 512$ .

For this purpose, we choose a case with a stronger forcing magnitude than any case studied in the validation section (A14-Cxy-S18 for  $\epsilon_* = 0.25$ ). The stronger magnitude results in steeper gradients and, thus, a more conservative set-up choice.

The domain size is completely determined by the simulation time  $T_*$  and the length  $L_{y_*}$ , which is the semi-domain height, but also sets the upstream and downstream fetch. All runs for the convergence study are conducted for  $T_* = 256$ , which is the longest simulation time used for the model validation. The angle of attack time dependence on  $L_{y_*}$  is shown in figure 27, where the grid size of the most inner refinement is  $\epsilon_*/\Delta x_* = 4$  and spans  $-4\epsilon_* < x_* < T_* + 4\epsilon_*$  and  $-4\epsilon_* < y_* < 4\epsilon_*$ . It can be seen that the angle of attack evolution is only smooth up to the time instance  $t_*$  where the start-up vortex reaches the location  $x_* \approx L_{y_*}$  and its induced velocity field, which scales with the inverse of the distance to the vortex core, is altered by the slip boundary conditions applied at the domain top and bottom. Consequently, we choose  $L_{y_*} = 256$  since we conduct validation LES runs with  $T_* = 256$ . The relative error compared with an even larger domain with  $L_{y_*} = 512$  (figure 27b) slowly increases with time but does not exceed 0.1 %, even at the final time instance  $t_* = T_*$ .

Furthermore, the resolution of the most inner refinement is varied between  $\epsilon_*/\Delta x_* = 2$ ,  $\epsilon_*/\Delta x_* = 4$  and  $\epsilon_*/\Delta x_* = 8$  using the chosen  $L_{y_*} = 256$ . Note that the resolution of the base grid is constant, and the resolution is varied by adding additional refinement levels around the actuator point and the wake region. The normal extent of the most inner refinement is always  $-4\epsilon_* < y_* < 4\epsilon_*$ . The streamwise extent of the two coarser resolutions is  $-4\epsilon_* < x_* < T_* + 4\epsilon_*$ , whereas the highest resolution case only adds an additional refinement level between  $-4\epsilon_* < x_* < 16 + 4\epsilon_*$ . The evolution of the angle of attack on these three different grid resolutions is shown in figure 28. Contrary to the domain size convergence, the relative angle of attack error for the grid resolution convergence stays constant after the start-up phase. This is the case because it is governed by the strength of the start-up vortex, which is determined during the initial phase of the step response. The relative error for the  $\epsilon_*/\Delta x_* = 4$  case is below 0.25 % after the first few time steps (figure 28b). We conservatively choose here a resolution of  $\epsilon_*/\Delta x_* = 8$  for all model validation runs, which ensures fully converged LES results.

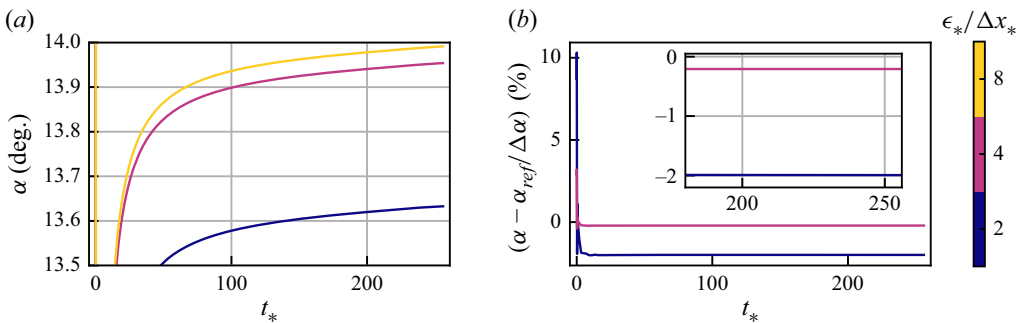


Figure 28. Grid size convergence study for case A14-Cxy-S18 using  $\epsilon_* = 0.25$ . The simulation time is  $T_* = 256$  and the semi-domain height is  $L_{y_*} = 256$ . (a) Angle of attack for the range of grid resolutions  $\epsilon_*/\Delta x_* = 2$  to  $\epsilon_*/\Delta x_* = 8$  (for the most inner refinement). The semi-domain height for all three cases is  $L_{y_*} = 256$ . (b) Relative error based on the angle of attack step magnitude  $\Delta\alpha = 18^\circ$ . The reference case for the calculation of the error is  $\epsilon_*/\Delta x_* = 8$ .

## REFERENCES

- ALMGREN, A.S., BELL, J.B., COLELLA, P., HOWELL, L.H. & WELCOME, M.L. 1998 A conservative adaptive projection method for the variable density incompressible Navier-Stokes equations. *J. Comput. Phys.* **142** (1), 1–46.
- ATASSI, H.M. 1984 The Sears problem for a lifting airfoil revisited - new results. *J. Fluid Mech.* **141**, 109–122.
- BATCHELOR, G.K. 1967 *An Introduction to Fluid Dynamics*. Cambridge University Press.
- BIRNBAUM, W. 1924 Das ebene problem des schlagenden Flügels. *ZAMP - J. Appl. Maths Mech. Z. Angew. Math. Mech.* **4** (4), 277–292.
- BISPLINGHOFF, R.L., ASHLEY, H. & HALFMAN, R.L. 1996 *Aeroelasticity*. Dover Publications.
- BRETON, S.-P., SUMNER, J., SØRENSEN, J.N., HANSEN, K.S., SARMAST, S. & IVANELLI, S. 2017 A survey of modelling methods for high-fidelity wind farm simulations using large eddy simulation. *Phil. Trans. R. Soc. A Math. Phys. Engng Sci.* **375** (2091), 20160097.
- CAPRACE, D.-G., CHATELAIN, P. & WINCKELMANS, G. 2019 Lifting line with various mollifications: theory and application to an elliptical wing. *AIAA J.* **57** (1), 17–28.
- CAPRACE, D.-G., WINCKELMANS, G. & CHATELAIN, P. 2020 An immersed lifting and dragging line model for the vortex particle-mesh method. *Theor. Comput. Fluid Dyn.* **34** (1), 21–48.
- CHURCHFIELD, M.J., LEE, S., MICHALAKES, J. & MORIARTY, P.J. 2012 A numerical study of the effects of atmospheric and wake turbulence on wind turbine dynamics. *J. Turbul.* **13**, N14.
- CHURCHFIELD, M.J., SCHRECK, S.J., MARTÍNEZ-TOSSAS, L.A., MENEVEAU, C. & SPALART, P.R. 2017 An advanced actuator line method for wind energy applications and beyond. In *35th Wind Energy Symposium*. American Institute of Aeronautics and Astronautics.
- DAĞ, K.O. 2017 Combined pseudo-spectral / actuator line model for wind turbine applications. PhD thesis, DTU Technical University of Denmark.
- DAĞ, K.O. & SØRENSEN, J.N. 2020 A new tip correction for actuator line computations. *Wind Energy* **23** (2), 148–160.
- FORSYTHE, J.R., LYNCH, E., POLSKY, S. & SPALART, P. 2015 Coupled flight simulator and CFD calculations of ship airwake using Kestrel. In *53rd AIAA Aerospace Sciences Meeting*. American Institute of Aeronautics and Astronautics.
- FREDERIK, J.A., DOEKEMEIJER, B.M., MULDERS, S.P. & VAN WINGERDEN, J.W. 2020 The helix approach: using dynamic individual pitch control to enhance wake mixing in wind farms. *Wind Energy* **23** (8), 1739–1751.
- GARRICK, I.E. 1938 On some reciprocal relations in the theory of nonstationary flows. *Tech. Rep.* 629. National Advisory Committee for Aeronautics.
- GOLDSTEIN, M.E. & ATASSI, H. 1976 A complete second-order theory for the unsteady flow about an airfoil due to a periodic gust. *J. Fluid Mech.* **74** (4), 741–765.
- HODGKIN, A., LAIZET, S. & DESKOS, G. 2022 Numerical investigation of the influence of shear and thermal stratification on the wind turbine tip-vortex stability. *Wind Energy* **25** (7), 1270–1289.
- IVANELLI, S., MIKKELSEN, R., SØRENSEN, J.N. & HENNINGSON, D. 2010 Stability analysis of the tip vortices of a wind turbine. *Wind Energy* **13** (8), 705–715.

- JHA, P.K. & SCHMITZ, S. 2018 Actuator curve embedding – an advanced actuator line model. *J. Fluid Mech.* **834**, R2.
- JONKMAN, J., BUTTERFIELD, S., MUSIAL, W. & SCOTT, G. 2009 Definition of a 5-MW reference wind turbine for offshore system development. *Tech. Rep. NREL/TP-500-38060*. National Renewable Energy Laboratory, Golden, CO.
- KLEINE, V.G., HANIFI, A. & HENNINSON, D.S. 2023a Non-iterative vortex-based smearing correction for the actuator line method. *J. Fluid Mech.* **961**, A29.
- KLEINE, V.G., HANIFI, A. & HENNINSON, D.S. 2023b Simulating airplane aerodynamics with body forces: actuator line method for nonplanar wings. *AIAA J.* **61** (5), 2048–2059.
- KLEUSBERG, E., BENARD, S. & HENNINSON, D.S. 2019 Tip-vortex breakdown of wind turbines subject to shear. *Wind Energy* **22** (12), 1789–1799.
- KUHN, M.B. et al. 2025 AMR-wind: a performance-portable, high-fidelity flow solver for wind farm simulations. *Wind Energy* **28** (5), e70010.
- VON KÁRMÁN, T. & SEARS, W.R. 1938 Airfoil theory for non-uniform motion. *J. Aeronaut. Sci.* **5** (10), 379–390.
- KÜSSNER, H.G. 1936 Zusammenfassender Bericht über den instationären Auftrieb von Flügeln. *Luftfahrtforschung* **13**, 410–424.
- LA CRUZ, W., MARTÍNEZ, J.M. & RAYDAN, M. 2006 Spectral residual method without gradient information for solving large-scale nonlinear systems of equations. *Maths Comput.* **75** (255), 1429–1448.
- LEISHMAN, J.G. 2002a Challenges in modelling the unsteady aerodynamics of wind turbines. *Wind Energy* **5** (2–3), 85–132.
- LEISHMAN, J.G. 2002b *Principles of Helicopter Aerodynamics*, 1st edn. Cambridge University Press.
- LEISHMAN, J.G. & BEDDOES, T.S. 1989 A semi-empirical model for dynamic stall. *J. Am. Helicopter Soc.* **34**, 3–17.
- LIMACHER, E.J. 2025 Towards a general theory of accelerating foils in the attached-flow regime. *J. Fluid Mech.* **1012**, R1.
- LIU, L., FRANCESCHINI, L., OLIVEIRA, D.F., GALEAZZO, F.C.C., CARMO, B.S. & STEVENS, R.J.A.M. 2022 Evaluating the accuracy of the actuator line model against blade element momentum theory in uniform inflow. *Wind Energy* **25** (6), 1046–1059.
- MACKOWSKI, A.W. & WILLIAMSON, C.H.K. 2015 Direct measurement of thrust and efficiency of an airfoil undergoing pure pitching. *J. Fluid Mech.* **765**, 524–543.
- MARTÍNEZ-TOSSAS, L.A., ALLAERTS, D., BRANLARD, E. & CHURCHFIELD, M.J. 2024 A solution method for the filtered lifting line theory. *J. Fluids Engng* **147** (011502), 011502-1–011502-8.
- MARTÍNEZ-TOSSAS, L.A., CHURCHFIELD, M.J. & LEONARDI, S. 2015 Large eddy simulations of the flow past wind turbines: actuator line and disk modeling. *Wind Energy* **18** (6), 1047–1060.
- MARTÍNEZ-TOSSAS, L.A. & MENEVEAU, C. 2019 Filtered lifting line theory and application to the actuator line model. *J. Fluid Mech.* **863**, 269–292.
- MARTÍNEZ-TOSSAS, L.A., SAKIEVICH, P., CHURCHFIELD, M.J. & MENEVEAU, C. 2024 Generalized filtered lifting line theory for arbitrary chord lengths and application to wind turbine blades. *Wind Energy* **27** (1), 101–106.
- MARTÍNEZ-TOSSAS, L.A., CHURCHFIELD, M.J. & MENEVEAU, C. 2017 Optimal smoothing length scale for actuator line models of wind turbine blades based on Gaussian body force distribution. *Wind Energy* **20** (6), 1083–1096.
- MENDOZA, V., BACHANT, P., FERREIRA, C. & GOUDÉ, A. 2019 Near-wake flow simulation of a vertical axis turbine using an actuator line model. *Wind Energy* **22** (2), 171–188.
- MEYER FORSTING, A.R., PIRRUNG, G.R. & RAMOS-GARCÍA, N. 2019a A vortex-based tip/smearing correction for the actuator line. *Wind Energy Sci.* **4** (2), 369–383.
- MEYER FORSTING, A.R., PIRRUNG, G.R. & RAMOS-GARCÍA, N. 2019b The wake of an actuator line with a vortex-based tip/smearing correction in uniform and turbulent inflow. *J. Phys.: Conf. Ser.* **1256** (1), 012020.
- MEYERS, J., BOTTASSO, C., DYKES, K., FLEMING, P., GEBRAAD, P., GIEBEL, G., GÖÇMEN, T. & VAN WINGERDEN, J.W. 2022 Wind farm flow control: prospects and challenges. *Wind Energy Sci.* **7** (6), 2271–2306.
- MILNE-THOMSON, L.M. 1973 *Theoretical Aerodynamics*, 4th edn. Dover Publications.
- MOTTA, V., GUARDONE, A. & QUARANTA, G. 2015 Influence of airfoil thickness on unsteady aerodynamic loads on pitching airfoils. *J. Fluid Mech.* **774**, 460–487.
- NING, S.A. 2014 A simple solution method for the blade element momentum equations with guaranteed convergence. *Wind Energy* **17** (9), 1327–1345.

- PORTE-AGEL, F., BASTANKHAH, M. & SHAMSODDIN, S. 2020 Wind-turbine and wind-farm flows: a review. *Boundary-Layer Meteorol.* **174** (1), 1–59.
- PRANDTL, L. 1924 Über die entstehung von Wirbeln in der idealen flüssigkeit, mit anwendung auf die tragflügeltheorie und andere aufgaben. In *Vorträge Aus Dem Gebiete der Hydro- Und Aerodynamik (Innsbruck 1922)* (ed. T.v. Kármán & T. Levi-Civita), pp. 18–33. Springer.
- SAFFMAN, P.G. 1992 *Vortex Dynamics*. Cambridge University Press.
- SANDERSE, B., PIJL, S.P. & KOREN, B. 2011 Review of computational fluid dynamics for wind turbine wake aerodynamics: review of CFD for wind turbine wake aerodynamics. *Wind Energy* **14** (7), 799–819.
- SARMAST, S., DADFAR, R., MIKKELSEN, R.F., SCHLATTER, P., IVANELLI, S., SØRENSEN, J.N. & HENNINGSON, D.S. 2014 Mutual inductance instability of the tip vortices behind a wind turbine. *J. Fluid Mech.* **755**, 705–731.
- SCHOLLENBERGER, M., LUTZ, T. & KRÄMER, E. 2020 Boundary condition based actuator line model to simulate the aerodynamic interactions at wingtip mounted propellers. In *New Results in Numerical and Experimental Fluid Mechanics XII* (ed. A. Dillmann, G. Heller, E. Krämer, C. Wagner, C. Tropea & S. Jakirlić), pp. 608–618. Springer International Publishing.
- SEARS, W.R. 1941 Some aspects of non-stationary airfoil theory and its practical application. *J. Aeronaut. Sci.* **8** (3), 104–108.
- SHARMA, A. *et al.* 2024 ExaWind: open-source CFD for hybrid-RANS/LES geometry-resolved wind turbine simulations in atmospheric flows. *Wind Energy* **27** (3), 225–257.
- SHEN, W.Z., SØRENSEN, J.N. & MIKKELSEN, R. 2005 Tip loss correction for actuator/Navier–Stokes computations. *J. Solar Energy Engng* **127** (2), 209–213.
- SHIVES, M. & CRAWFORD, C. 2013 Mesh and load distribution requirements for actuator line CFD simulations. *Wind Energy* **16** (8), 1183–1196.
- STANLY, R., MARTÍNEZ-TOSSAS, L.A., FRANKEL, S.H. & DELORME, Y. 2022 Large-eddy simulation of a wind turbine using a filtered actuator line model. *J. Wind Engng Ind. Aerodyn.* **222**, 104868.
- SØRENSEN, J.N., MIKKELSEN, R.F., HENNINGSON, D.S., IVANELLI, S., SARMAST, S. & ANDERSEN, S.J. 2015 Simulation of wind turbine wakes using the actuator line technique. *Phil. Trans. R. Soc. A Math. Phys. Engng Sci.* **373** (2035), 20140071.
- SØRENSEN, J.N. & SHEN, W.Z. 2002 Numerical modeling of wind turbine wakes. *J. Fluids Eng.* **124** (2), 393–399.
- TASCHNER, E., FOLKERSMA, M., MARTÍNEZ-TOSSAS, L.A., VERZIJLBERGH, R. & VAN WINGERDEN, J.W. 2024 A new coupling of a GPU-resident large-eddy simulation code with a multiphysics wind turbine simulation tool. *Wind Energy* **27** (11), 1152–1172.
- THEODORSEN, T. 1935 General theory of aerodynamic instability and the mechanism of flutter. *Tech. Rep. 496*. National Advisory Committee for Aeronautics.
- TROLDBORG, N. 2009 Actuator line modeling of wind turbine wakes. PhD thesis, DTU Technical University of Denmark.
- TROLDBORG, N., LARSEN, G.C., MADSEN, H.A., HANSEN, K.S., SØRENSEN, J.N. & MIKKELSEN, R. 2011 Numerical simulations of wake interaction between two wind turbines at various inflow conditions. *Wind Energy* **14** (7), 859–876.
- TROLDBORG, N., SORENSEN, J.N. & MIKKELSEN, R. 2010 Numerical simulations of wake characteristics of a wind turbine in uniform inflow. *Wind Energy* **13** (1), 86–99.
- VEERS, P. *et al.* 2019 Grand challenges in the science of wind energy. *Science* **366** (6464), 1–9.
- VIRTANEN, P. *et al.* 2020 SciPy 1.0: fundamental algorithms for scientific computing in Python. *Nat. Meth.* **17** (3), 261–272.
- WAGNER, H. 1925 Über die Entstehung des dynamischen Auftriebes von Tragflügeln. *ZAMM - J. Appl. Maths Mech. Z. Angew. Math. Mech.* **5** (1), 17–35.
- YILMAZ, A.E. & MEYERS, J. 2018 Optimal dynamic induction control of a pair of inline wind turbines. *Phys. Fluids* **30** (8), 085106.
- ÖTOMO, S., HENNE, S., MULLENERS, K., RAMESH, K. & VIOLA, I.M. 2020 Unsteady lift on a high-amplitude pitching aerofoil. *Exp. Fluids* **62** (1), 6.